Encapsulation Methods of Sulfur Particles for Lithium-Sulfur Batteries: A Review

Shiqi Li [a, *], Zhaoyang Fan [b, **]

[a] College of Electronic Information, Hangzhou Dianzi University, Hangzhou, 310018, China.

[b] Department of Electrical and Computer Engineering and Nano Tech Center, Texas Tech University, Lubbock, Texas 79409, USA.

[*] Corresponding author. [**] Corresponding author.

E-mail addresses: sqli@pku.edu.cn (S. Li); zhaoyang.fan@ttu.edu (Z. Fan).

Abstract

Core-shell structured sulfur nanoparticles (NPs) and their various derivatives have been widely investigated as a promising cathode material for Li-S batteries (LSBs) thanks to their unique features in suppressing the lithium polysulfides shuttle effect, accommodating the sulfur electrode volume change, and providing abundant electrochemically active sites. The commonly used infiltration strategy falls short in producing a near ideal core-shell structure. Accordingly, the strategy of encapsulation, in which the prefabricated sulfur or sulfur precursor nanocore is encapsulated by a subsequently formed host shell has attracted broad interest, and this technique has significantly accelerated the LSB development. To advance the state of the art in producing encapsulated sulfur NPs, it becomes necessary to systematically survey the past relevant works and sum up research gaps. This review first takes an excursion to the infiltration strategy to highlight its limitations, followed by surveys on studies of synthesizing sulfur NPs, encapsulating sulfur NPs, and producing encapsulated sulfur NPs from metal sulfides. The strengths and weaknesses of each method, the resulted NPs, their electrochemical properties and the associated LSB performances are particularly emphasized. The rationales to

design and the results of applying structural derivatives of the conventional core-shell configuration are then assessed. The encapsulated sulfur NPs applied in aqueous batteries are also discussed. This comprehensive review on sulfur encapsulation is concluded by a summary on further challenges and opportunities as well as our perspectives on possible future research directions, towards fundamental understanding and practical development of encapsulated sulfur NP-based LSB technology.

Key words: composite cathodes, lithium-sulfur batteries, lithium metal anodes, polysulfides, electrolytes

1. Introduction

Li-S chemistry is regarded as a near-future battery technology that could deliver a specific energy more than 350 Wh kg^{-1}, surpassing the state-of-the-art Li-ion battery (LIB) technology [1-3]. In contrast to the one-electron Li-ion chemistry, Li-S battery (LSB) features a two-electron based redox reaction per sulfur atom: $S_8 + 16\ Li^+ + 16\ e^- \leftrightarrow 8\ Li_2S$, where crystalline α-S_8, or *cyclo*-octasulfur, is the most thermodynamically stable sulfur allotrope [4, 5]. During the discharge process, S_8 undergoes a reduction process through multiple long-chain lithium polysulfide intermediates (Li_2S_x, $3 < x \leq 8$, or LiPSs) into Li_2S_2 and Li_2S, releasing a theoretical specific capacity of 1675 mAh g^{-1}, several folds higher than the intercalation transition-metal-oxide-based cathode [6, 7]. Owing to its earth abundance (17^{th} richest element), low production

cost (~ $200 per metric ton), and less toxicity, sulfur will also help reduce the battery cost and contribute to sustainable and environmentally benign battery technology development.

Although a large body of work has been done, a practical LSB technology is still illusive, mainly caused by the low sulfur utilization and the rapid capacity deterioration. In addition to attacking problems associated with the lithium metal anode, great attention has been focused on the improvement of the poor sulfur cathode performance. The very low electronic and ionic conductivities of solid elemental sulfur, lithium disulfide (Li_2S_2) and lithium sulfide (Li_2S) give rise to sluggish redox reaction kinetics and low sulfur utilization. A large volumetric fluctuation of the electrode during charge and discharge further exacerbates the cathode stability issue. Perhaps the most notorious problem associated with LSB is the shuttle effects arising from dissolution of LiPSs in ether-based electrolytes and their diffusion between the cathode and the anode [8-11]. It is noted that ether-based electrolytes are necessary since LiPSs easily react with carbonate-based solvents.

The possibility of using the Li-S redox pair for batteries was envisioned in the early 1970s. Early researches concentrated on using the vapor or molten sulfur as the electrode material together with solid electrolytes. Ambient-temperature rechargeable LSBs were not considered commercially viable until the middle of 1990s. Broad interest in this field was sparked by the innovative work from Nazar's group to confine LiPSs in a mesoporous carbon host [12]. Since then, a large variety of carbonaceous materials have been introduced into the sulfur cathode design to enhance their electronic conductivity and mitigate their volume fluctuation while ameliorating the shuttle effect of LiPSs via physical traps. Subsequently, heteroatom-doped porous carbon hosts with a polar surface were developed to simultaneously physically confine

and chemically bond LiPSs [13-16]. Analogously, transition metal oxides, nitrides, and sulfides, as well as polymers with polar groups, among others, have been blended into a carbon matrix to host sulfur, demonstrating improved electrochemical performance [17, 18]. Particularly, some of these materials also serve as electrocatalysts by stabilizing LiPSs on the electrode surface and reducing the activation energy to accelerate the conversion of sulfur species, thus further suppressing the diffusion and shuttle effects of LiPSs [19]. These efforts have greatly improved the LSB performance.

To deliver a specific energy surpassing the state-of-the-art LIBs, LSBs must possess a large sulfur content and a large mass loading [20-23]. A cathode host with an open porous structure, which immobilizes the LiPSs mainly through its surface, hardly fulfill such a prerequisite. A more effective strategy in restraining LiPSs from diffusing out of the cathode is to encapsulate them within a lithium permeable shell. Such a structure prevents the outward diffusion of LiPSs more effectively by entrapping them inside the shells and thus it could attain high sulfur content and mass loading when properly designed [24]. Simultaneously, the hollow structure can also provide extra void space in the core and mechanical strength via its shell to accommodate the volume expansion of the active materials during discharge. The encapsulated sulfur nanoparticles (NPs) can also be easily adapted in the conventional slurry casting process for electrode manufacturing. With these merits, it is not a surprise that carbonaceous hollow structures, including hollow carbon spheres (HCSs) [25-33], hollow carbon nanocubes [34], hollow carbon nanorods [35], carbon nanotubes [36, 37], and others [38], have been investigated to host sulfur. Similarly, polymers [39-41], metal chalcogenides [42-52], metal nitrides [53], metal hydroxides [54, 55], and their composites with carbon [56-69], have also

been engineered into hollow structures to host sulfur, offering combined merits of physical and chemical confinement of LiPSs and electrocatalytic conversion of sulfur species. Such a core-shell structure therefore allows a sulfur cathode design with much improved performances.

In the literature, two generic strategies can be differentiated in terms of how to prepare the core-shell particles. In one, the sulfur species are infiltrated into prefabricated hollow host particles, and in the other, prefabricated sulfur or sulfur precursor NPs are subsequently encapsulated by a host shell. For the infiltration strategy, an obvious challenge lies at how to infiltrate a large amount of sulfur material into a well-sealed shell. Although not so accurately, one could argue that a shell structure that allows sulfur to be easily infiltrated into will also permit it to easily diffuse out from. Therefore, this strategy intrinsically has its severe limitations and falls short in implementing the inherent merits of the core-shell encapsulated structure. In this context, a better strategy, that is, forming a host shell that encapsulates the prefabricated sulfur or sulfur precursor NPs has been pursued and developed, which is the main subject of this review.

In this article, we will first survey the several methods for synthesizing sulfur NPs (Section 3), and then assess different approaches to encapsulate them (Section 4), followed by a survey on carbon coated sulfur NPs derived from encapsulated metal sulfides (Section 5). Derivatives from the conventional core-shell structures are then covered in Section 6. In the survey, the relationships between the morphology/structure of encapsulated sulfur NPs, their electrochemical properties and the associated LSB performance are particularly examined. In Section 7, the progress on encapsulated sulfur NPs applied in aqueous batteries is discussed. This review is concluded with a summary on further challenges and opportunities, and our

perspectives on possible future works are especially emphasized towards further performance improvement (Section 8).

Before we proceed to the main subjects on the encapsulation strategy, we will take an excursion to the infiltration strategy in order to understand its limitations.

2. The infiltration strategy and its limitations

Melt-diffusion, dissolution-diffusion, and vapor-phase infusion are the three popular methods that have been pursued to infiltrate sulfur species into prefabricated host hollow NPS.

2.1 Melt-diffusion method

The melt-diffusion method has been widely used by many research groups. Specifically, a hollow structure is first prepared and then melted sulfur is infiltrated through pores across the shell into the hollow space via capillary action. After cooling down, the infiltrated sulfur solidifies and aggregates in the core [70-73]. Although infiltrated sulfur was presumed to locate in the core of the hollow structure and indeed this is the case in a few reports (Figure 1 (a)-(c)) [45, 74-79], in many other studies sulfur particles were mainly found dispersed throughout the tiny shell pores but not in the core volume (Figure 1 (d)-(e)) [27, 62, 80-83]. Some authors argued that sulfur never filled into the hollow core because of either the absence of driving forces for sulfur to pass through the shell during the melt-diffusion process, or the shell pores simply being blocked or disconnected [83], while others deemed that the small amount of infiltrated sulfur, when observed under an electron microscope, simply sublimed in its ultrahigh vacuum, further exacerbated by the electron beam heating [84, 85]. Both mechanisms could also be jointly responsible for the observation of the absence of sulfur in the core of the particles

[80].

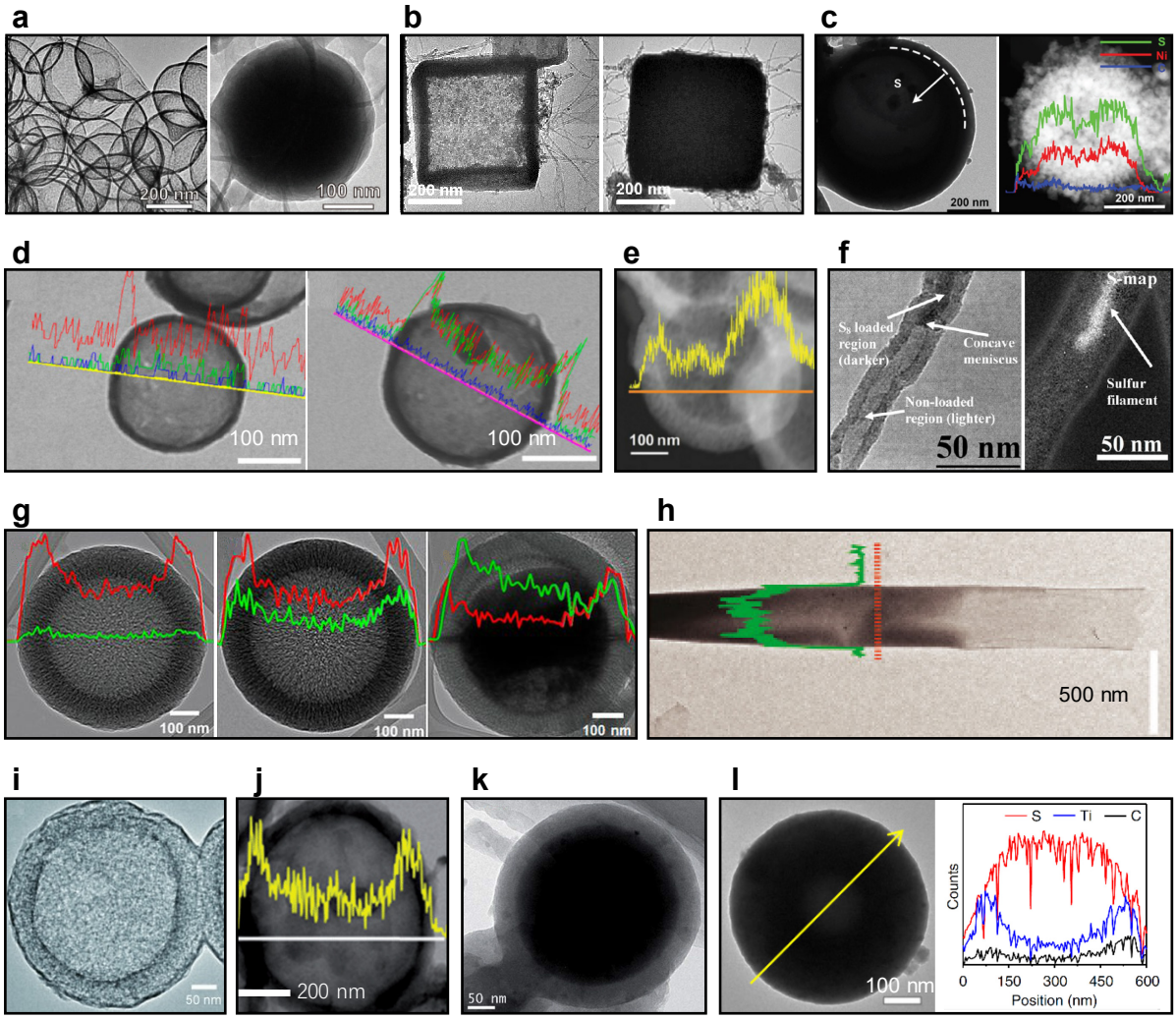

Figure 1. (a) TEM images of HCSs before (left) and after (right) filling with sulfur [77]. Reproduced with permission from Wiley. (b) TEM images of hollow Co_3S_4 nanoboxes before (left) and after (right) filling with sulfur [45]. Reproduced with permission from American Chemical Society. (c) TEM (left) and STEM (right) images of nano-sized NiS decorated HCSs after filling with sulfur [63]. The inset shows the line scan analysis of elements. Reproduced with permission from Wiley. (d) TEM images and line scan analysis (red-carbon, green-sulfur)

of sulfur-filled HCSs with 70% sulfur (left) and 80% sulfur (right) [83]. Reproduced with permission from American Chemical Society. (e) TEM images and line scan analysis (yellow-sulfur) of sulfur-filled carbon nitride-based spheres [80]. Reproduced with permission from Wiley. (f) TEM image (left) of a sulfur-filled carbon nanotube and the sulfur element mapping (right) [86]. Reproduced with permission from American Chemical Society. (g) TEM image and line scan analysis (red-carbon, green-sulfur) of sulfur-filled HCSs via dissolution-diffusion with CS_2 (left), CS_2/IPA (middle), and CS_2/NMP (right) as the solvent, respectively [87]. Reproduced with permission from National Academy of Sciences. (h) TEM image and line scan analysis (green-sulfur) of a sulfur-filled carbon nanotube via combined dissolution- and melt-diffusion [88]. Reproduced with permission from American Chemical Society. (i) TEM image of an individual sulfur-filled HCS [89]. Reproduced with permission from Wiley. (j) STEM image of sulfur-filled PANI sphere and its line scan analysis (yellow-sulfur) [40]. Reproduced with permission from Royal Society of Chemistry. (k) TEM image of an individual sulfur-filled HCS [90]. Reproduced with permission from Royal Society of Chemistry. (l) TEM image of an individual sulfur-filled hollow titanium monoxide@carbon sphere [91]. Line scan analysis is also included in (l). Reproduced with permission from Nature Publishing Group.

A noticeable study reported pore size effect on the sulfur sublimation in vacuum and suggested that small nanopores in the shell might well protect sulfur from sublimation [84]. HCSs with different pore sizes of 4.1, 3.2, and 2.8 nm were used to host sulfur. When the pore size was 2.8 nm, the sulfur was not only impregnated into the HCSs, but also stable under electron microscope observation. In contrast, when the pore size was 3.2 or 4.1 nm, the sulfur

easily sublimed. This observation might be described by the Barret-Joyner-Halenda theory [92], which states that when a substance is confined in a porous material, its vapor pressure drops due to capillary condensation, and the smaller the pore is, the lower the vapor pressure will be. This study suggests that it is critical to design the shell with small nanopores for protecting sulfur species. Not surprisingly, such a shell in fact, is also conducive for sulfur infiltration via the capillary action.

According to the Young-Laplace equation of capillary action, the height (h) up to which a liquid will rise is described as $h = \frac{2\gamma \cos\theta}{\rho g r}$, where γ, θ, ρ, g, and r represent the surface tension of the melted sulfur, the contact angle between the sulfur liquid and the host material, the density of the sulfur liquid, the acceleration of gravity, and the diameter of the pore, respectively [86]. Although the wicking length of the melted sulfur does not necessarily strictly follow this equation considering that they can migrate along shell pores with arbitrary orientations, it still could be appreciated that the wicking length is determined by both the pore size and the contact angle between the melted sulfur and the host surface. A sulfophilic shell with narrow pores would facilitate sulfur filling into the hollow core, while a polar host surface and wide pores impede the inward migration. In this sense, the functionalized carbon surface to enhance chemical binding of LiPSs, in fact, retards the inward diffusion of sulfur. Typically, melted sulfur exhibits only partial wetting on the carbon surface with a contact angle of approximately 50° [93]. It should also be emphasized that even though a small pore diameter enhances the capillary diffusion, the pore size must be large enough to accommodate sulfur molecules with S-S bond length in the range of 0.189-2.066 nm [94]. Studies on the hollow core filling process, either via simulation or *in-situ* experimental observation, are still scarce,

while such studies are needed to guide the porous shell design for easier infiltration of sulfur while tightly blocking outward diffusion of LiPSs.

The hollow core with little or no sulfur infiltrated into will not contribute to the capacity and the sulfur confinement. In order to facilitate sulfur impregnation, the structure of hollow spheres can be modified to reduce the migration distance from the shell surface into the hollow core. Examples are grid-like multicavity carbon spheres [95] and hollow indented carbon spheres [96]. Modification of the melt-diffusion method was also implemented by introducing or applying extra migration driving forces. For instance, core-shell or yolk-shell carbon spheres with voids between the core or yolk and the shell demonstrated increased driving forces for sulfur impregnation than conventional hollow carbon spheres [97, 98]. Noticeably, Dutta et al. developed a pressure-induced capillary filling method to drive sulfur into carbon nanotubes (Figure 1 (f)), and achieved an exceptionally stable sulfur cathode with a sulfur content and a sulfur loading of 84% and 10 mg cm^{-2}, respectively [86].

A serious problem of the melt-diffusion method is the accumulation of a large amount of sulfur on the shell external surface, and thus the goal to confine sulfur species in a closed shell cannot be fulfilled [75, 83, 98, 99]. A further treatment is needed to dissolve the surface sulfur in a solvent or evaporate it at a high temperature (such as 300 ℃) [96, 98]. However, the sulfur loading is then further adversely affected.

2.2 Dissolution-diffusion method

Dissolution-diffusion is a method similar to melt-diffusion except that sulfur is not melted but dissolved in a solvent. This method also relies on the capillary force to drive the dissolved sulfur into small pores. Carbon disulfide (CS_2) and toluene are common solvents to dissolve

sulfur [100, 101]. In order to increase the driving force, isopropyl alcohol (IPA) or *N*-methyl-2-pyrrolidone (NMP) can be blended with CS_2, since they exhibit 1.4 and 1.7 times larger capillary pressure than CS_2, respectively. Figure 1 (g) compares the effect of solvents on sulfur impregnation [87]. With the capillary pressure increasing, more sulfur specie was infiltrated into the hollow core. Hollow carbon nanofibers were also filled with sulfur by combining the dissolution- and melt-diffusion methods, as shown in Figure 1 (h) [69, 88].

2.3 Vapor-phase infusion method

Vapor-phase infusion is another method to impregnate sulfur into a hollow structure [89-91, 102-107]. Specifically, solid sulfur is evaporated under high temperatures in a confined space, and the vapor diffuses into hollow hosts and then nucleates via capillary condensation. In some references, no sulfur aggregates were found in the core (Figure 1 (i)-(j)) [40, 89], while in other cases, the otherwise hollow space was well occupied by sulfur (Figure 1 (k)-(l)) [90, 91]. Sulfur filling by this vapor-phase infusion method has not been well studied. Like the aforementioned two methods, condensation of the sulfur vapor on the external particle surface cannot be avoided and a further treatment is still needed to remove the surface sulfur [91, 102].

2.4 Short comments

Briefly speaking, exciting progress has been made in constructing sulfur cathodes by infiltrating sulfur into prefabricated hollow structures using either the melt-diffusion, the dissolution-diffusion, or the vapor-phase-infusion method. The strength of this infiltration strategy lies that the low-cost sulfur powder is directly used as the sulfur source to infiltrate into a hollow shell to form the core-shell nanostructure, and hence it does not need a laborious step to fabricate sulfur NPs. However, this strategy falls short in filling the hollow core with

enough sulfur if a highly sealed shell is used. When a prefabricated hollow structure is easier to be filled, it must also allow easier diffusion of LiPSs out of the shell. On the other hand, a tightly sealed prefabricated hollow structure will unavoidably be wreaked by a low sulfur loading and hence a low energy density. In addition, this strategy does not allow other sulfur precursors that have high melting points and low solubilities to be used.

Facing these challenges, a second strategy—encapsulating prefabricated sulfur or sulfide/disulfide NPs—have attracted considerable interest in recent years, which is the focus of this review article. But first, we will survey the various methods to prepare sulfur NPs.

3. Production of sulfur NPs

Commercially available sulfur powders have irregular shapes and non-uniform sizes in the range of 5-15 μm [108]. They are directly used as the sulfur source to infiltrate into the prefabricated hollow particles. However, for the strategy of encapsulating sulfur particles, regular shapes, preferably spherical sulfur NPs should be prepared first. Large sulfur particles would be detrimental to electron and lithium ion transport as well as volume expansion accommodation. This is particularly true at high discharge rates where a high Li^+ concentration at the sulfur particle surface will form an insulating Li_2S_2/Li_2S blocking layer, impeding utilization of subsurface sulfur [109]. Downscaling sulfur particle size to nanoscale will shorten the electron and ion transport distances and enable full utilization of the active material as well as contributing to high charge/discharge rates [109]. Therefore, the first step of encapsulation is to attain sulfur NPs. Different methods for synthesizing sulfur NPs will be surveyed in this section. They are divided into two categories: $Na_2S_2O_3$-based synthesis and elemental sulfur-based synthesis.

3.1 $Na_2S_2O_3$-based synthesis

A popular method to produce monodispersed hollow sulfur nanospheres is to react sodium thiosulfate ($Na_2S_2O_3$) and acid at room temperature in the presence of polyvinylpyrrolidone (PVP). The latter forms micelles as a soft template guiding the synthesis of hollow sulfur nanospheres [108, 110-119]. The synthesis follows the reaction of $Na_2S_2O_3 + 2\ H^+ \rightarrow S\downarrow + SO_2\uparrow + 2\ Na^+ + H_2O$. Such formed sulfur nanospheres have a diameter of around 500 nm with a hollow core and a porous surface (Figure 2 (a)). The small surface pores were generated from SO_2 bubbles in the synthesis. The hollow core and the small surface pores help accommodate the volume expansion of sulfur particles during discharge [110, 115], thus avoiding disjointing of the active material from the cathode and maintaining its integrity. PVP with a higher molecular weight would more readily produce nanopores on the surface of hollow sulfur spheres [115], which further tune their electrochemical performance. The powder X-ray diffraction (XRD) pattern of these sulfur nanospheres was indexed to the orthorhombic phase of sulfur [111 112], showing no difference from the commercial sulfur source.

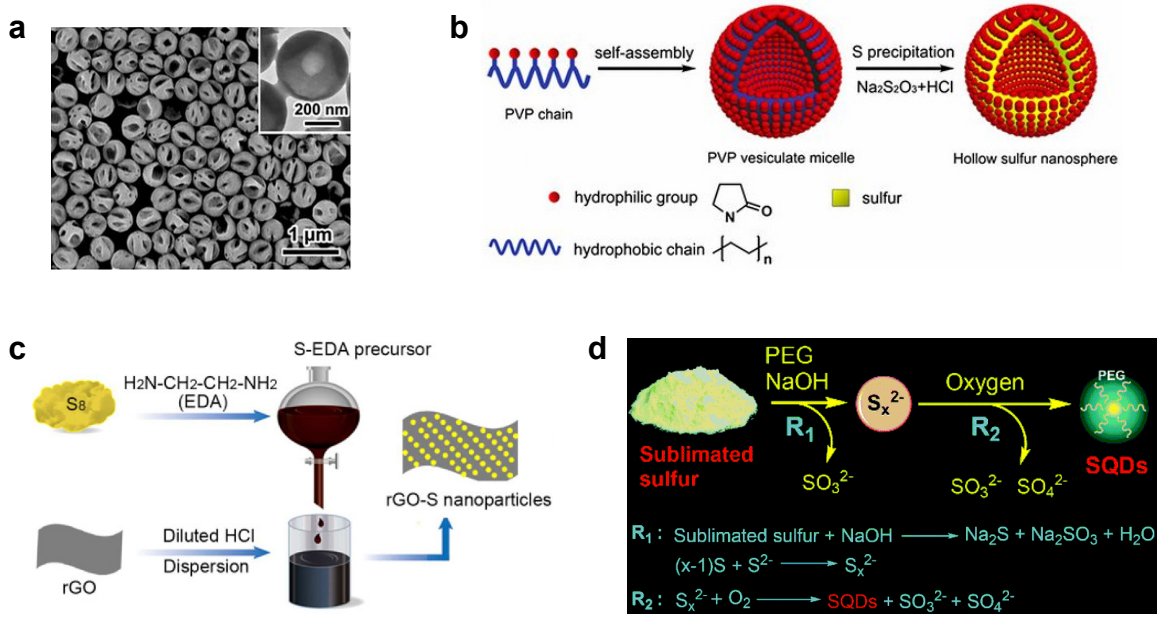

Figure 2. (a) SEM image of the hollow sulfur nanospheres. The inset shows the TEM image of an individual hollow sulfur nanosphere [110]. Reproduced with permission from National Academy of Sciences of the United States of America. (b) A schematic to illustrate the formation mechanism of the hollow sulfur nanospheres [110]. Reproduced with permission from National Academy of Sciences of the United States of America. (c) A schematic to illustrate the synthesis process of sulfur NPs via the sulfur-amine chemistry [109]. Reproduced with permission from American Chemical Society. (d) A schematic to illustrate the formation mechanism of SQDs [120]. Reproduced with permission from Royal Society of Chemistry.

The formation mechanism of hollow sulfur nanospheres is schematically illustrated in Figure 2 (b). Amphiphilic PVP molecules are composed of hydrophobic nonpolar alkyl backbone and hydrophilic polar lactam group [121]. In an aqueous solution, PVP molecules are linked together with their nonpolar alkyl backbones pointed back on to the water and the polar lactam group toward the water, forming hollow spherical micelles with a bilayer structure,

similar as that of the conventional lipid bilayer and micelles [110, 121]. Hydrophobic sulfur will preferentially grow onto the hydrophobic portion of PVP micelles, thereby forming hollow nanospheres. Monodispersed hollow sulfur nanospheres with a similar diameter around 500 nm can also be achieved by selecting polyvinyl alcohol (PVA) or polydiallyldimethylammonium chloride (polyDADMAC) as soft templates which have a similar structural configuration as PVP, while polyethylene glycol (PEG) cannot assist the formation of sulfur nanospheres since PEG cannot self-organize into the bilayer and micelle structure [110].

Sulfur nanospheres have also been synthesized by using Triton X-100 as the surfactant, with a size (> 1 μm) larger than that obtained by using PVP as the surfactant [122, 123]. Nevertheless, there is no evidence indicating that they have a hollow core, although Triton X-100 molecules also consist of a hydrophobic hydroxyl groups and a hydrophilic poly(ethylene glycol) chain. The size difference between sulfur spheres formed by the assistance of PVP and Triton X-100 is determined by their micelle sizes.

Besides nanospheres, small sulfur particles with different morphologies have also been achieved by other synthesis via controlling the reacting temperature or surfactants. For instance, diamond-shaped sulfur NPs with a short diagonal of 450 nm were achieved by reacting $Na_2S_2O_3$ and acid at 0 ℃ in the presence of PVP, in comparison with sulfur nanospheres at room temperature [124]. Fu et al. prepared monodispersed bi-pyramidal sulfur particles with a size around 3 μm by reacting $Na_2S_2O_3$ and HCl at room temperature in the presence of decyltrimethylammonium bromide (DeTAB) [125]. Its XRD pattern also indicates the orthorhombic phase of sulfur [125]. The mechanism of forming diamond or bi-pyramidal

shapes was not discussed.

3.2 Elemental sulfur-based synthesis

Commercial sulfur sources are mainly produced as a by-product in oil refining and natural gas purification [126]. More than 60 million tons of sulfur are produced every year [127], providing a low-cost raw material.

Dissolution-recrystallization is a facile physical method to transform microscale sulfur powder to NPs. Sulfur is dissolved in solvents, such as CS_2, toluene, ethanol, or acetone, and then recrystallized when the solvent is evaporated to achieve sulfur NPs [88, 128-131]. For instance, Chen et al. synthesized sulfur NPs with a diameter of 10-20 nm via a unique membrane-assisted dissolution-recrystallization technique [132]. Specifically, S/CS_2 solution is added to PVP/ethanol through a microfiltration membrane where they form micro-droplets. As sulfur is slightly soluble in ethanol, the sulfur will precipitate into NPs as soon as the S/CS_2 micro-droplets contact with the ethanol. Meanwhile, PVP serves as wrapping ligands to prevent aggregation of the formed sulfur NPs. Recycling the used CS_2 or toluene solvent to minimize environment impact should be achievable. Xie et al. synthesized sulfur nanorods with a typical diameter of around 80 nm and an average aspect ratio of 6-8 by dissolving sulfur powder in a green solvent, PEG-200 [133]. PEG-200 serves as both a solvent to dissolve the raw sulfur and a structure-directing agent to control the size, morphology and stability of the product. The formation of sulfur nanorods could be explained by the Ostwald ripening and oriented attachment theory.

Sulfur particles can not only recrystallize in an oversaturated solution, but also on surfaces of carbon materials [129, 130, 134]. For instance, sulfur NPs were recrystallized as a coating

on CNTs as the acetone or ethanol/water solvent in the sulfur/CNTs suspension vaporized [130, 134]. The density functional theory (DFT)-based calculations by Fan et al. revealed that the adsorption interaction between S_8 and CNTs is stronger than that between two S_8 rings [130]. Thus, CNTs serve as the heterogeneous nucleating centers for sulfur recrystallization on their surface. Besides dissolution-recrystallization treatment, raw sulfur could also be converted to sulfur NPs on carbonaceous materials by melt-diffusion or vapor-phase infusion [135, 136].

Mechanical milling is another physical method to achieve sulfur NPs [137, 138]. Sulfur NPs as small as 10 nm were achieved by ball milling sulfur powder for 48 hours [137]. This procedure is time- and energy-consuming, and the size distribution of the achieved sulfur particles is not homogeneous.

Chemical methods are also investigated to convert microscale sulfur powder to NPs. Chen's group developed sulfur-amine chemistry to synthesize sulfur NPs, as shown in Figure 2 (c) [109, 139]. Specifically, elemental sulfur is first reacted with ethylenediamine (EDA) to form a S-EDA complex precursor which is then slowly added to a diluted hydrochloric acid (HCl) solution. The S-EDA precursor decomposes in the HCl solution and sulfur NPs are recovered. Monodispersed sulfur NPs with a diameter ranging from 150, 40, 20, 10 to 5 nm were prepared by adjusting reaction conditions such as deposition time and the solution pH [109]. Using this method, the composites of sulfur NPs with reduced graphene oxide (RGO) and CNTs were prepared [109, 139].

Sulfur can react with sodium sulfide (Na_2S) to generate sodium polysulfide (Na_2S_x), which can then produce small sulfur particles in the presence of acid through the disproportionation reaction [140-144]: $S_x^{2-} + 2\ H^+ \rightarrow (x-1)\ S\downarrow + H_2S\uparrow$. The role of surfactant was validated: as

with Triton X-100 added, sulfur nanospheres with a diameter around 150 nm were achieved; otherwise it was several micrometers [140].

Recently, sulfur quantum dots (SQDs) with a diameter of several nanometers, which show excellent aqueous dispersibility, have been reported by simply treating sublimated sulfur with alkali at 70-90 ℃ using PEG as passivation agents [120, 145-151]. The high resolution TEM (HRTEM) images and XRD patterns imply that the spacing between the two adjacent lattice planes and the corresponding diffraction peaks of these SQDs are different from orthorhombic S_8 phase, which might be caused by their amorphous nature [149, 150]. The Raman spectra of SQDs are in accordance with that of sublimed sulfur powder, confirming SQDs are sulfur material [150]. Song et al. revealed the formation mechanism of SQDs [120]. As shown in Figure 2 (d), S_x^{2-} is first generated by the reaction of sulfur and NaOH, which then reacts with O_2 to form zero-valent sulfur, and further assembles into SQDs with the assistance of PEG. Oxygen and PEG are two key factors in the synthesis of SQDs. The yield of SQDs prepared under an O_2 atmosphere with a reaction time of 10 h reached as high as 5.08%, in comparison with 0.87% of that prepared under an air atmosphere with a reaction time of even 60 h [120]. In contrast, no SQDs were obtained under an Ar atmosphere [120]. The PEG at the SQDs surface could effectively prevent their aggregation and ensure their excellent stability in water [148]. So far studies of SQDs focus on their optical properties [151-153], while there has been no reports on their application in electrochemical energy storage. In consideration of their ultra-small size, it is reasonable to assume that they may act as an ideal sulfur source to construct sulfur cathodes in overcoming the reaction kinetics for high-rate performance. Their low synthesis yield, however, must be solved for practical LSB application.

4. Encapsulation of sulfur particles

According to the used shell material, the various encapsulation methods, as discussed in this section, are categorized into polymer-, metal-, sulfide-, oxide-, and transition metal hydroxide-based encapsulation. Our survey focuses on the relation between the morphology/structure of the encapsulated sulfur particles and their electrochemical performance.

4.1 Polymer-based encapsulation

To reveal the detailed structure of the synthesized hollow sulfur nanospheres using self-organized PVP templates, Li et al. heated them in vacuum and analyzed their morphology evolution under SEM to confirm the existence of the PVP shell [110]. The core-shell structured S@PVP spheres delivered an initial specific capacity of 990 mAh g^{-1} and exhibited reasonable cycling stability with a degradation rate of only 0.046% per cycle during 1,000 cycles, which were attributed to the PVP encapsulation function and the reserved void space in the core of the sulfur nanospheres [110]. It deserves to be mentioned that although their existence has been verified [110, 111, 118], the PVP shells were not either observed or particularly emphasized in other works using a similar synthesis method [108, 112-117, 154]. The disparity might be related to the different concentrations of reactants or PVP and the different rinsing conditions used in synthesis. As confirmed by Li et al., PVP shells could be easily removed from the surface of the hollow sulfur nanospheres by water rinse [110].

Although a PVP shell can provide protection, the high resistance of PVP causes relatively poor rate performance for S@PVP spheres. Other polymers with relatively high electronic

and/or ionic conductivities have been attempted as a shell material to encapsulate sulfur NPs. These include polypyrrole (PPY) [122, 140, 155-157], polyaniline (PANI) [113, 158, 159], poly(3,4-ethylenedioxythiophene) (PEDOT) [110, 124, 132], polythiophene (PTh) [160], and polydopamine (PDA) [115, 119, 135]. The encapsulating process is called as an *in situ* chemical oxidative polymerization process. Specifically, the monomers, such as pyrrole, aniline, 3,4-ethylenedioxythiophene (EDOT), thiophene, and dopamine, are first blended with the aqueous suspension of sulfur NPs, and then polymerized through oxidation by added oxidants, such as $(NH_4)_2S_2O_8$, $FeCl_3$, or the oxygen in the atmosphere. Figure 3 (a) shows TEM images of sulfur nanospheres encapsulated by PPY (S@PPY), by PANI (S@PANI), by PEDOT (S@PEDOT), and by PDA (S@PDA), respectively. The polymer coating on the sulfur nanosphere could be clearly identified. After encapsulation, the monodispersity and the spherical morphology of sulfur nanospheres were well preserved. The encapsulated sulfur NPs showed enhanced electrochemical performance over those without a polymer coating. For instance, the S@PEDOT cathode delivered an initial specific capacity of 1,093 mAh g^{-1}, and retained 551 mAh g^{-1} after 200 cycles, in comparison with an initial capacity of 626 mAh g^{-1}, and only 83 mAh g^{-1} retained after 200 cycles for sulfur nanospheres without a PEDOT coating [112].

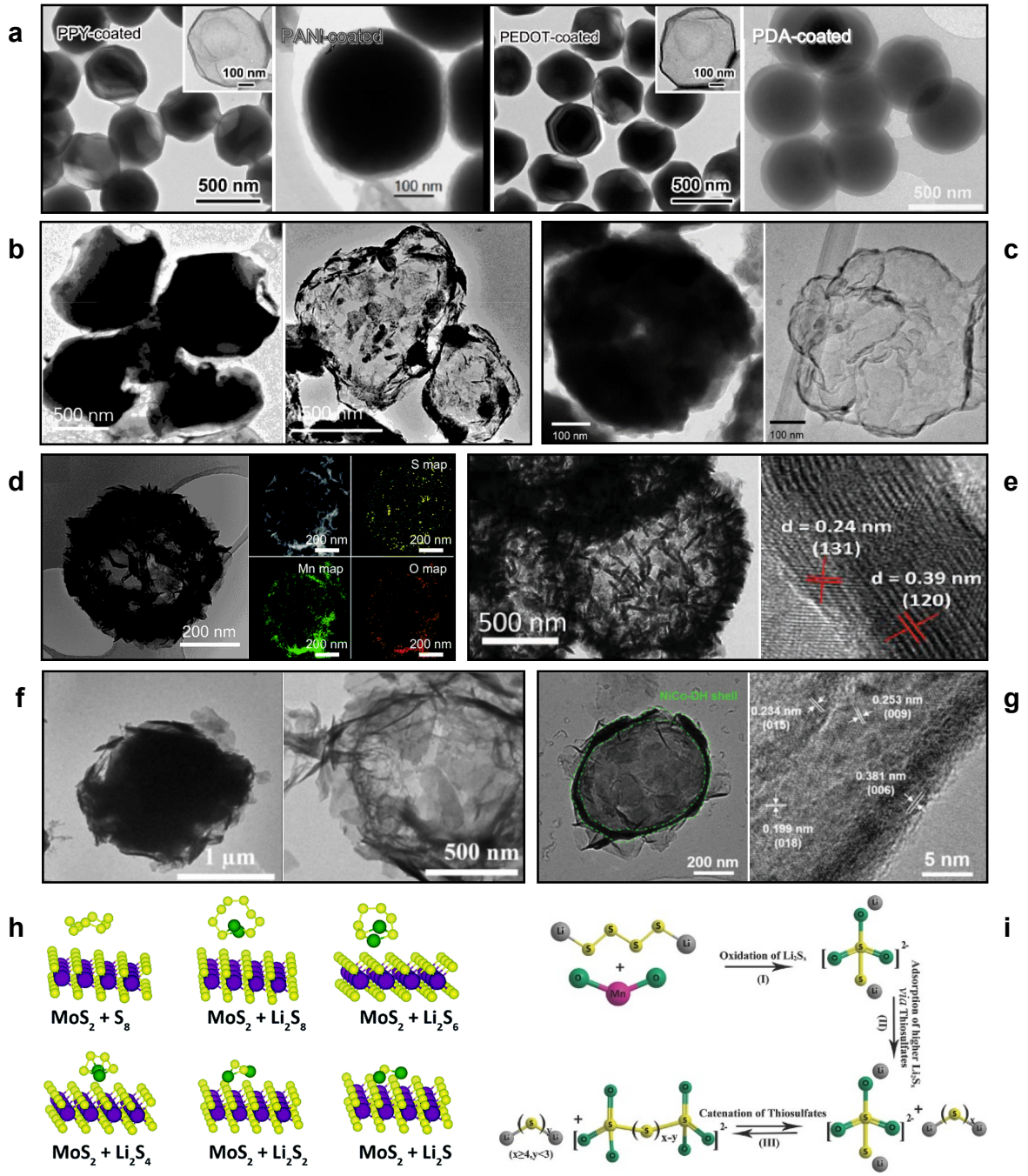

Figure 3. (a) TEM image of S@PPY [161], S@PANI [113], S@PEDOT [161], and S@PDA [115]. Reproduced with permission from American Chemical Society and Elsevier. (b) TEM image of S@Ga (left) and its Ga shell after sulfur removal (right) [162]. Reproduced with permission from Royal Society of Chemistry. (c) TEM image of S@MoS_2 (left) and its MoS_2 shell after sulfur removal (right) [118]. Reproduced with permission from American Chemical

Society. (d) TEM image (left) and dark field STEM image with EDS map of element S, Mn, O (right) of S@δ-MnO_2 [111]. Reproduced with permission from Royal Society of Chemistry. (e) TEM image of S@γ-MnO_2 (left) and HRTEM image of γ-MnO_2 nanorods (right) [117]. Reproduced with permission from Wiley. (f) TEM image of S@$Co(OH)_2$ (left) and its $Co(OH)_2$ shell after sulfur evaporated under TEM observation (right) [163]. Reproduced with permission from American Chemical Society. (g) TEM image of S@NiCo-DH (left) and HRTEM image of the NiCo-DH shell (right) [164]. Reproduced with permission from Wiley. (h) A schematic illustrating various polysulfide conformations on MoS_2 [165]. Reproduced with permission from Royal Society of Chemistry. (i) A schematic illustrating the interaction between polysulfides and MnO_2 [166]. Reproduced with permission from Wiley.

Due to easy implementation, a large body of works have been done to encapsulate sulfur NPs with a polymer coating. Generally speaking, encapsulation using a polymer has the following benefits:

1) The polymer coating, attained simultaneously in the sulfur NP synthesis process, helps prevent NPs from aggregation. For instance, with the chemical oxidative polymerization of pyrrole simultaneously proceeding, sulfur particles with an average diameter of around 100-200 nm encapsulated by PPY were achieved; in contrast, without PPY, the synthesized sulfur particles exhibited an average diameter of around 3-5 μm [122].

2) Some polymers can improve the electronic and/or lithium ionic conductivities of the sulfur cathode, as PPY, PANI, PEDOT, and PTh have a relatively high electronic conductivity [112, 121, 160, 167, 168], and PDA, abundant of catechol and amine groups, facilitates Li^+

transport due to their strong absorbing capability of liquid electrolytes [115, 119, 135]. In the electrode, polymer shells are linked together to form an electronically or ionically conductive network, thereby compensating the poor electronic and ionic conductivity of sulfur and Li_2S_2/Li_2S. As verified by electrochemical impedance spectroscopy (EIS) measurements, the PEDOT and PTh coating largely reduced the charge-transfer resistance [132, 160].

3) The shell serves as a physical barrier to retard the diffusion of LiPSs. DFT-based calculations and X-ray photoelectron spectroscopy (XPS) characterizations suggest that chemical interactions exist between PDA and LiPSs and Li_2S_2/Li_2S, thereby hindering the detachment of Li_2S_2/Li_2S and alleviating the LiPSs shuttle effect [115]. The lone electron pairs on the electronegative oxygen and nitrogen atoms in PDA bind with the Li atoms in LiPSs and Li_2S_2/Li_2S, forming coordination-like interactions (O…Li, N…Li, and O…Li…N) [115]. DFT-based calculations also show that a stable chemical bind is created between PEDOT and sulfur species [169]. With their abundant oxygen or nitrogen atoms, it is reasonable to think that the chemical bonding also exists between the other three polymers (PPY, PANI, PTh) and sulfur species. Li et al. have comparatively studied the chemical bonding between Li_xS ($0 < x \leq 2$) and PPY, PANI, PEDOT via DFT-based calculations, and found that PEDOT has stronger interaction than PPY and PANI with Li_xS [161]. In addition, EIS measurements indicated the conductivities of the three polymers decrease in the order of PEDOT > PPY > PANI. Accordingly, PEDOT coating showed more obvious effects in enhancing the cycling stability, Coulombic efficiency, and rate capability of sulfur cathodes than the other two [161].

4) The experimental results showed that even after sulfur sublimation, the polymer shells remained intact [110, 115]. It is thus believed that the tenacious polymer coating, thanks to its

high mechanical flexibility and good adhesion capability, helps buffer the volume change of the sulfur cathode, so that the outward diffusion of LiPSs could be effectually alleviated, and intimate contact between sulfur species and host materials could be maintained.

A relatively thick polymer coating is more conducive to enhancing the specific capacity and cycling stability [161], and the coating thickness can be easily adjusted by changing the self-polymerization time or the concentration of monomers [115, 119]. The negative effects that may result from a thick coating should also be evaluated, such as a low sulfur content, sluggish Li^+ conduction, and more electrolyte needed for wetting the cathode. Accordingly, a polymer coating with a moderate thickness is preferred to serve as a valid barrier for soluble LiPSs, but not to degrade other performance [132].

In addition to *in situ* chemical oxidative polymerization, Muldoon's group developed a layer-by-layer (LBL) technique to encapsulate sulfur/carbon cores with a polyelectrolyte multilayer (PEML) membrane [170, 171]. Another method to encapsulate sulfur/carbon composite with a polymer is simply mixing them together. As polymers can easily form a homogeneous and compact surface layer on the sulfur/carbon composite, the outward diffusion of LiPSs were effectively alleviated [172-175]. Since these two methods are mainly applied to sulfur/carbon composites rather than individual sulfur NPs, these will be discussed in detail in Section 6.1.

4.2 Metal-based encapsulation

With their excellent electronic conductivity and metallic ductility, metals logically become a candidate to encapsulate sulfur particles [176]. Leveraging on the low melting point (29.8 °C)

of gallium (Ga), core-shell structured S@Ga composite was synthesized by mixing liquid Ga and sulfur NPs [162]. Figure 3 (b) clearly shows the S@Ga core-shell structure and the Ga shell after sulfur removal. Further characterizations demonstrate that an ultra-thin Ga_2S_3 film was created between the sulfur core and the Ga shell during the mixing process, which helps balance the difference in surface energies of sulfur and Ga and enables sulfur NPs coated by the Ga shell. When S@Ga NPs applied in the cathode, the Ga shell not only enhances the electronic conductivity of the electrode, but also restrains the outward dissolution of LiPSs. In addition, the integrity of the electrode is well retained as the liquid Ga shell perfectly adapts to the volume change of the sulfur nanoparticle during charge/discharge process thanks to its superior plasticity. This self-adaptivity ensures a superior contact between the sulfur species and the electronic/ionic conductors (including the Ga shell, the conductive additive, and the electrolyte). Accordingly, the S@Ga composites exhibited an excellent cycling stability with a fading rate of only 0.043% per cycle at 1 C during 1,000 cycles [162].

A layer of Ag film with a thickness of 67 nm was coated on sulfur nanospheres to enhance their electronic conductivity [154]. In this process, $SnCl_2$ was introduced to the colloidal solution of sulfur nanospheres, followed by addition of $AgNO_3$. The formation of Ag coating is ascribed to the reduction of Ag^+ by Sn^{2+} via the reaction: $Sn^{2+} + 2\ Ag^+ \rightarrow 2\ Ag + Sn^{4+}$, and the preferred heterogeneous crystallization of Ag on sulfur particles in the presence of Sn^{2+} [154]. Further characterizations found that a trace amount of SnO_x (x = 1 or 2) also exists in the coating layer due to the hydrolysis of Sn^{2+} and Sn^{4+}, followed by the dehydration of resulted $Sn(OH)_2$ and $Sn(OH)_4$. Both the chemical bonding between SnO_x and LiPSs and the physical confinement resulting from the shell structure are conducive to alleviating the shuttle effect

[177]. This coating strategy shows great flexibility as it not only applies to sulfur nanospheres, but also to commercially available large sulfur particles, and their electrochemical performance were both enhanced after this treatment [154].

Despite their high electronic conductivity, metal coatings suffer from their high mass densities, and lack of chemical binding with LiPSs.

4.3 Sulfide-based encapsulation

MoS_2 has attracted great attention for application in LSBs due to its fascinating properties. The approach to composite MoS_2 and sulfur had been limited to melt-diffusion until the innovative work by Tang et al [118]. As MoS_2 flakes are capable of self-assembling to form hollow and highly conformal cages in the presence of PVP, a facile method was developed to encapsulate sulfur nanospheres with MoS_2 flakes simply by dispersing PVP encapsulated sulfur nanospheres in solution containing MoS_2 flakes under stirring at room temperature [118]. Figure 3 (c) shows the TEM images of S@MoS_2 and the MoS_2 shell after sulfur removal, clearly indicating that the sulfur nanosphere is hermetically encapsulated by a MoS_2 shell. The MoS_2 coating enables the S@MoS_2 to withstand 200 kV electron irradiation under high vacuum ($\sim 10^{-7}$-10^{-9}) for more than 3 h, which was ascribed to the strong van der Waals force between MoS_2 nanoflakes, their high flexibility, and their hermetically sealing effect. In contrast, naked sulfur particles quickly sublimed in 4 min under vacuum [118]. Based on the first-principles molecular dynamics simulation, the smallest solvated lithium polysulfide possesses a size of 5.71 Å, which is much bigger than the interlayer space between MoS_2 layers (around 3 Å) [118]. Accordingly, the MoS_2 coating shows the possibility to physically trap the

soluble LiPSs. The DFT calculation results imply that the binding energies between sulfur species (Li_2S_8, Li_2S_6, Li_2S_4, Li_2S_2, and Li_2S) and MoS_2 are 0.10, 0.22, 0.32, 0.65, and 0.87 eV, respectively, higher than that between sulfur species and carbon [165]. The strong binding capability of the MoS_2 substrate roots from its chemical interaction with Li atoms in sulfur species (Figure 3 (h)) [165], which helps suppress the diffusion of dissolved LiPSs. In addition, the defects and vacancies in MoS_2, such as MoS_2 edge sites, serve as an electrocatalyst to promote the kinetics of polysulfide conversion, thereby decreasing their accumulation in the catholyte and further inhibiting their subsequent loss by diffusion [178, 179]. MoS_2 flakes also demonstrate impressive mechanical stability when applied as a sulfur host, as the elastic constants of MoS_2 along the C_{11} and C_{12} axial direction increase along with the amount of anchored Li_2S [165]. In addition, the as-formed wrinkles on the MoS_2 cages provide extra space for sulfur cathode volume expansion during discharge. It deserves to be mentioned that upon lithiation, the semiconducting 2H-MoS_2 is partially transformed into the metallic 1T' phase with a high electronic conductivity of 10-100 S cm^{-1}, which will facilitate the electron conduction in the sulfur cathodes [118]. Owing to these merits, the S@MoS_2 core-shell NPs retained a specific capacity of 956 mAh g^{-1} after 300 cycles under 0.5 C, in comparison with only 570 mAh g^{-1} retention for sulfur nanospheres without a MoS_2 coating.

Another metal sulfide, $FePS_3$ also receives tremendous attention due to its large surface area and abundant active sites arising from its layered structural characteristics [180]. Similar to MoS_2 flakes, exfoliated $FePS_3$ flakes tend to encapsulate sulfur nanospheres when the two are mixed in a solution [181]. Thanks to the confinement of LiPSs from the $FePS_3$ shell, the core-shell structured S@$FePS_3$ exhibited excellent cycling stability with a fading rate of only

0.046% per cycle during 1,000 cycles under 1 C. The chemical interaction between the $FePS_3$ shell and the sulfur species has yet to be investigated to quantitatively reveal the mechanisms responsible for the much-enhanced performance.

Using layered transition metal sulfide flakes to coat sulfur NPs offers the merits of structural stability, efficient physical trapping and chemical binding of otherwise diffused LiPSs, and the improved redox reaction rate contributed from their catalytic function. However, their typically large mass density has adverse impact on the electrode specific energy.

4.4 Oxide-based encapsulation

With the assistance of a soft or hard template, the hydrolysis of titanate or titanium salt and tetraethyl orthosilicate (TEOS) can be exploited to synthesize TiO_2 and SiO_2 hollow spheres, respectively [182-184]. Along this way, sulfur nanospheres have been encapsulated by TiO_2 shells (30 nm in thickness) or SiO_2 shells (20 nm in thickness) through the hydrolysis of titanium diisopropoxide bis(acetylacetonate) (or TDB), and TEOS, respectively [185, 186]. Besides as a physical barrier to LiPSs outward diffusion, TiO_2 and SiO_2 tend to chemically absorb LiPSs due to their abundance of Ti-O or Si-O groups, and surface hydroxyl groups [183, 187, 188]. Consequently, TiO_2- and SiO_2- coated sulfur nanospheres both exhibited enhanced electrochemical performance compared with naked sulfur nanospheres [185, 186]. However, the application of TiO_2 and SiO_2 in sulfur cathodes may be plagued by their poor electronic conductivity as well as their low surface area and high mass density.

In comparison with TiO_2 and SiO_2, MnO_2 is a more popular material to encapsulate sulfur particles. Birnessite-type MnO_2 (δ-MnO_2) nanosheets were coated on sulfur nanospheres by

reducing potassium permanganate ($KMnO_4$) on sulfur nanospheres [108]. The reaction is interpreted as [108, 189]: $6\ MnO_4^- + 3\ S + H_2O \rightarrow 6\ MnO_2 + SO_4^{2-} + [H(SO_4)_2]^{3-} + OH^-$. Both nanoscale and microscale sulfur particles can be coated via this method, showing its great flexibility. As PDA and PVP are capable of reducing some noble metal ions owing to their functional groups such as o-quinone, carboxy, amino, imine, and phenol groups, the δ-MnO_2 shell can also be formed via the reaction between $KMnO_4$ and the PDA or PVP layer initially coated on the sulfur particles [111, 116]. For instance, core-shell structured S@PDA was first synthesized by *in situ* polymerization of dopamine on sulfur nanospheres, and then the PDA shell served as a reductant and sacrificial template to transform $KMnO_4$ into δ-MnO_2 shell [116]. The thickness of the δ-MnO_2 shell could be well controlled by adjusting the thickness of PDA shell that is mainly determined by the concentration of dopamine in the reaction solution. Tuning the δ-MnO_2 shell thickness is beneficial for controlling the sulfur content in the composite and balancing physical confinement with electron/ion transport. As shown by the TEM images of δ-MnO_2 and the corresponding EDS mapping of element S, Mn, O (Figure 3 (d)), sulfur locates in the core, and the δ-MnO_2 shell is composed of nanosheets, which will facilitate electrolyte wettability.

Reactions between $KMnO_4$ and sulfur, and between $KMnO_4$ and PDA, and the polymerization of dopamine, all are carried out under mild condition, including ambient pressure and temperature, suggesting the potential of this method for practical application with further consideration of low costs of sulfur, $KMnO_4$, and dopamine.

Except for physical confinement of LiPSs, introduction of the MnO_2 shell will bring two other benefits. One is that the chemical interactions between MnO_2 and sulfur species

immobilize the dissolved LiPSs. As discovered from DFT calculations [111], the interaction between sulfur species and MnO_2 is rooted from S=O or Li-O chemical bonds. Notably, after full lithiation, Li_2S is not stable and eventually decomposes into Li and S atoms with S=O and Li-O bonds on MnO_2 surface, which will facilitate its conversion to LiPSs and then to sulfur in the charge process. In addition to its chemical bonding function, MnO_2, serving as a polysulfide mediator, can further alleviate the shuttle effect [190]. Specifically, as shown in Figure 3 (i), thiosulfate groups ($S_2O_3^{2-}$) are first generated via the oxidation of LiPSs by MnO_2, which proceed to form polythionate complex ($S_xO_6^{2-}$) by catenating newly generated LiPSs and convert the latter to shorter chains of LiPSs. As the polythionates and the shorter chains of LiPSs are expected to be poorly soluble, this process is considered effectual to curtail the shuttle effect. The polysulfide mediator role of MnO_2 has also been validated by other groups [166, 191-193]. In consideration of its high specific surface area (123 $m^2\ g^{-1}$), MnO_2 shells are capable of providing abundant anchoring and conversion sites for LiPSs [108]. Therefore, the core-shell structured S@MnO_2 particles delivered much better electrochemical performance than both naked sulfur nanospheres and composites achieved by physically mixing commercial sulfur powder and MnO_2 nanosheets [111].

In addition to δ-MnO_2, nsutite-type MnO_2 (γ-MnO_2) was also coated on sulfur nanospheres by firstly dispersing the latter in an aqueous solution of manganese sulfate ($MnSO_4$), and then adding $KMnO_4$ to the solution [117]. The reaction is described as: $2\ KMnO_4 + 3\ MnSO_4 + 2\ H_2O \rightarrow 5\ MnO_2 + K_2SO_4 + 2\ H_2SO_4$. Different from δ-$MnO_2$ shells that are composed of nanosheets, the γ-MnO_2 shells exhibit a rough nanorod-covered surface, as shown in Figure 3 (e). The lattice spacings of 0.24 and 0.39 nm are attributed to the (131) and (120) planes of the

γ-MnO_2 phase, respectively (Figure 3 (e)). Similar to δ-MnO_2, γ-MnO_2 also chemically interacts with LiPSs and serves as a polysulfide mediator, thereby alleviating the shuttle effect. In addition, the γ-MnO_2 crystallographic form also provides one-dimensional tunnels for Li^+ intercalation to suppress insoluble Li_2S_2/Li_2S deposition at high discharge rates [117]. Thus, the S@γ-MnO_2 cathode might be better than the S@δ-MnO_2 cathode.

Due to the poor electronic conductivity of MnO_2, electronically conductive agents are needed for S@MnO_2 particles, which will further diminish the sulfur content in the cathode and ultimately result in a low specific energy. Besides, the surface phase evolution from γ-MnO_2 and δ-MnO_2 to Mn_3O_4 and the subsequent decomposition of Mn_3O_4 together with the dissociation of polysulfides, which is an irreversible process during discharge, might give rise to the capacity degradation of S@MnO_2 cathodes [117, 194].

In the community of LSB study, XPS, as a characterization tool, has been widely used to reveal the chemical bonds between host materials and sulfur species and to identify their reaction products. A recent study suggests that in the overwhelming majority of cases, an incorrect referencing of the binding energy scale was used [195]. Thus, we should be cautious on the conclusions drawn from XPS characterization.

4.5 Hydroxide-based encapsulation

Due to their unique morphology and abundance of hydrophilic groups, hollow transition metal hydroxide spheres are another category of materials widely applied to host sulfur using the melt-diffusion method [54, 55]. Similarly, *in-situ* formed transition metal hydroxide coating on sulfur particles have also been attempted.

During the hydrolysis of transition metal salts, transition metal hydroxide nanosheets are formed that are apt to encapsulate the nearby NPs. This tendency may be attributed to the electrostatic force between these hydroxide nanosheets [196, 197]. Accordingly, hollow transition metal hydroxide spheres are often synthesized by a sacrificial template method [54, 55]. Along this path, sulfur NPs could be encapsulated by a shell composed of transition metal hydroxides when the former are present in the precursor solution for the latter. For instance, a $Co(OH)_2$ layer or $Ni(OH)_2$ layer were uniformly coated on sulfur nanospheres by hydrolysis of cobalt or nickel salt, respectively [163, 198]. As shown in Figure 3 (f), such $Co(OH)_2$ layer is constructed from many nanosheets that loosely connect with each other at the edges on the surface of sulfur NPs, which not only serves as a physical barrier to trap the polysulfides, but also facilitates the transport of lithium ions and during discharge helps the accommodation of volume expansion. Thanks to the formation of metal-sulfur or lithium-hydroxyl bonds, the transition metal hydroxides show strong chemical adsorption to LiPSs [199, 200]. For instance, the binding energies between (101) plane of $Ni(OH)_2$ with Li_2S and Li_2S_4 were calculated to be -7.17 and -5.16 eV, respectively, which are much higher than those between RGO with Li_2S (-3.63) and Li_2S_4 (-3.21 eV) [201]. The combined physical confinement and chemical bonding functions of the transition metal hydroxide shell endow the corresponding sulfur cathode with enhanced electrochemical performance.

Besides $Co(OH)_2$ and $Ni(OH)_2$, the Ni-Co double hydroxide (NiCo-DH) shells were also coated on the as-prepared sulfur nanospheres via the simultaneous hydrolysis of cobalt and nickel salt [164]. As shown in Figure 3 (g), the nanosheets form a round shell, and the lattice spacings of 0.381, 0.253, 0.234, and 0.199 nm, are attributed to the (006), (009), (015), and

(018) planes of NiCo-DH, respectively. Compared with that based on $Ni(OH)_2$, NiCo-DH-based sulfur cathodes demonstrated higher specific capacity and Coulombic efficiency, and better cycling stability [164]. Zhang et al. explained this finding according to the "Goldilocks" principle put forward by Nazar's group [164]. When the redox potential (vs Li^+/Li) of the host ranges from 2.4 to 3.05 V, the polysulfides can be oxidized to thiosulfate which proceeds to form polythionate complex by catenating newly generated LiPSs and converts the latter to short-chain LiPSs [202]. This process not only provides anchoring sites of LiPSs, but also promotes their conversion kinetics, and finally contributes to significant suppression of the shuttle effect. In contrast, when the redox potential (vs Li^+/Li) of the host is higher than 3.05 V, LiPSs are oxidized to a mixture of sulfate and thiosulfate, and the electrochemically inert sulfate would passivate the electrode surface during charge/discharge process, resulting in poor cycling performance [202]. Thus, the difference in redox potentials between NiCo-DH (2.74 vs Li^+/Li) and $Ni(OH)_2$ (3.43 V vs Li^+/Li) leads to the huge difference in their electrochemical performance [164]. These studies suggest the crucial roles of the redox potentials of host materials in improving the sulfur cathode performance, which unfortunately has not caught enough attention in the community.

To sum up, the encapsulating strategies include polymerization of monomers, mixing sulfur particles and host materials, self-assembly of nanoflakes or chemical reactions (hydrolysis or redox) on the surface of sulfur NPs, as summarized in Figure 4. The encapsulating materials range from polymers to metals, sulfides, oxides, and hydroxides. In addition to physically and chemically confining sulfur species in the shells, some of them promote the electron transport in the sulfur cathodes due to their high electronic conductivities (Table 1), while others can

enhance the Li^+ conductivity in the sulfur cathode. A small number of the shell materials may also serve as electrocatalysts promoting the redox kinetics between sulfur species. Usually, a given shell structure may offer several functions.

Table 2 summarizes various shell materials used to encapsulate sulfur particles and the corresponding LSB electrochemical performance.

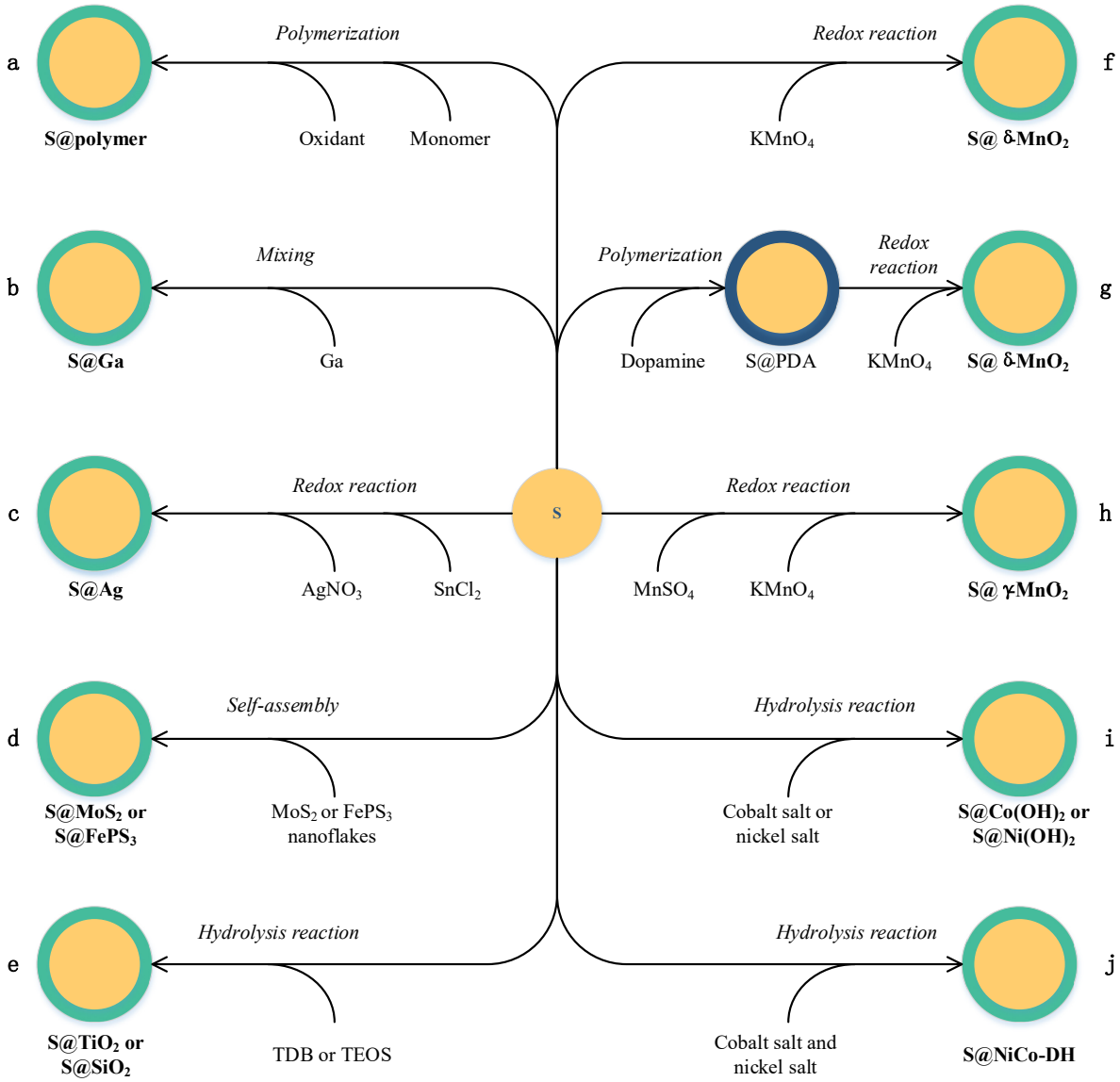

Figure 4. A schematic illustrating the encapsulation processes with various materials: (a)

Polymers, (b) Ga, (c) Ag, (d) MoS_2 or $FePS_3$, (e) TiO_2 or SiO_2, (f) and (g) δ-MnO_2, (h) γ-MnO_2, (i) $Co(OH)_2$ or $Ni(OH)_2$, and (j) NiCo-DH.

Table 1 The electronic conductivities of some shell materials.

Item	PPY	PANI	PEDOT	PTh	Ga	Ag
Electronic conductivity (S cm^{-1}) at 25 ℃	1.0 × 10^2	4.6 × 10^{-5}	1.5 × 10^3	1.0 × 10^3	3.7 × 10^4	6.3 × 10^5

Table 2 The various shell materials reported to encapsulate sulfur particles and their corresponding electrode performance.

Shell materials	Size of sulfur particles (nm)	Sulfur content (%)	Sulfur loading (mg cm^{-2})	Initial specific capacity (mAh g^{-1})	Cycling number @ cycling rate	Decay rate (%)	Ref.
PVP	400-500	49	1.0	990	1,000 @ 0.5 C	0.046	[110]
PPY	700	59.3	0.95	1,300	75 @ 0.2 C	0.373	[114]
PPY	150	64	2.6	1,142	100 @ 0.1 C	0.300	[140]
PPY	200-400	49.5	2.0	1,039	50 @ 0.1 C	0.820	[155]
PPY	400	53.9	1.5	1,201	500 @ 0.5 C	0.080	[161]
PANI	300	65.6	2.0	840	125 @ 0.2 C	0.530	[113]
PANI	300	54.2	1.8-3.0	1,198	100 @ 0.2 C	0.513	[158]
PANI	400	51.8	1.5	1,140	500 @ 0.5 C	0.110	[161]
PEDOT	500	65.3	-	1,093	200 @ 0.2 C	0.250	[112]
PEDOT	10-20	50.4	1.66	1,117	50 @ 0.25 C	0.335	[132]
PEDOT	400	54.6	1.5	1,165	500 @ 0.5 C	0.066	[161]
PTh	20,000	50.3	-	1,119	80 @ 0.06 C	0.323	[160]
PDA	500	59.8	1.2	1,048	200 @ 0.12 C	0.040	[115]
Ag	500-1,000	71.2	2.5	1,282	40 @ 0.2 C	0.647	[154]
Ga	900	56	1.5	500	200 @ 0.5 C	0.050	[162]
MoS_2	500	45.5	1.5	1,149	300 @ 0.5 C	0.056	[118]
$FePS_3$	500	56	0.56	1,080	1,000 @ 1 C	0.046	[181]
TiO_2	800	59	0.4-0.6	-	200 @ 0.5 C	0.170	[185]
SiO_2	700-800	54	-	1,050	50 @ 0.1 C	1.150	[186]
δ-MnO_2	300-400	68	1.5-1.7	1,050	300 @ 0.5 C	0.117	[108]
δ-MnO_2	300	56.6	1.7-2.1	1,110	1,000 @ 0.5 C	0.050	[111]

δ-MnO_2	600-800	47.1	1.0-1.3	1,200	200 @ 0.06 C	0.183	[116]
γ-MnO_2	500-600	42.7	2.0	936	300 @ 0.5 C	0.047	[117]
$Co(OH)_2$	500-700	64	3.3	1,283	50 @ 0.3 C	0.480	[163]
$Ni(OH)_2$	500	56	2.2	708	1,000 @ 1 C	0.040	[198]

5. Carbon coated sulfur particles derived from encapsulated metal sulfides

With a low melting point of 115.2 °C for sulfur, the encapsulation methods surveyed in Section 4 are limited to those carried out at or close to the room temperature. Since some sulfides or disulfides can endure much higher processing temperatures and they may also have a low solubility in water, another strategy can be employed to realize encapsulated sulfur NPs: first encapsulating sulfur precursor at a high temperature and then converting it into elemental sulfur particles. Metal sulfides or disulfides, such as cadmium sulfide (CdS) [203], zinc sulfide (ZnS) [204-208], iron disulfide (FeS_2) [209] and iron sulfide (FeS) [210], can be used as such a sulfur precursor. The merit of this strategy is that carbon, the best hosting material, can be deposited at a high temperature on the sulfur precursor particles. For instance, acetylene was decomposed to generate carbon coating on ZnS nanosheets at 900 ℃ [204]. Metallorganics including zinc dimethyldithiocarbamate, and iron (II) diethyl dithiocarbamate were treated at 750 ℃ to attain carbon coated ZnS and FeS particles, respectively [210, 211].

Considering the easier conformal coating of polymer on NPs, it is not surprising that carbonization of a polymer coating into a carbon coating is a more popular encapsulation method. Similar to encapsulating sulfur particles, the polymer encapsulating of metal sulfides/disulfides can be realized by mixing them together [205, 207, 209], or in situ polymerizing monomers [203, 206, 208]. Such polymers include PVP [209], phenol formaldehyde (PF) [207], resorcinol formaldehyde (RF) [205], and PDA [203, 206, 208],

which are then converted to a thin carbon coating after high temperature treatment. Compared with those containing only C, H, and O elements, polymers that also have nitrogen element will generate nitrogen doped carbon [206, 208]. As verified by theoretical calculations and nuclear magnetic resonance characterization, nitrogen dopants in carbon, especially pyridinic nitrogen, tend to create strong interaction with LiPSs through lithium bond, thereby effectively suppressing the shuttle effect and enhancing the utilization of sulfur species [212, 213]. Regarding another metal sulfide, sodium sulfide (Na_2S), even though it has a high solubility in water, glucose coated Na_2S crystals were attained via freeze-drying, followed by high-temperature treatment to convert glucose to carbon shells [214].

Such carbon coated metal sulfides/disulfides are then oxidized by oxidants such as Fe^{3+}, I_2, HNO_3, to achieve carbon coated sulfur. Figure 5 (a) schematically illustrates a typical process to prepare the carbon encapsulated sulfur NPs through this method. The sulfur content and the carbon shell thickness could be well controlled by changing the mass ratio of polymers to metal sulfides/disulfides in a solution synthesis or controlling the exposure duration of metal sulfides/disulfides to C_2H_2 in a gas phase synthesis [205, 214]. Such achieved sulfur/carbon hybrids were reported with different morphologies. For instance, Ding et al. found that such a hybrid presented a yolk-shell structure (Figure 5 (b)) [207, 211], while the sulfur particles were found firmly anchoring on the carbon inner shell by Wang et al [205]. It is worth noting that upon SEM or TEM observation, the sulfur particles may evaporate resulting in different observed morphologies.

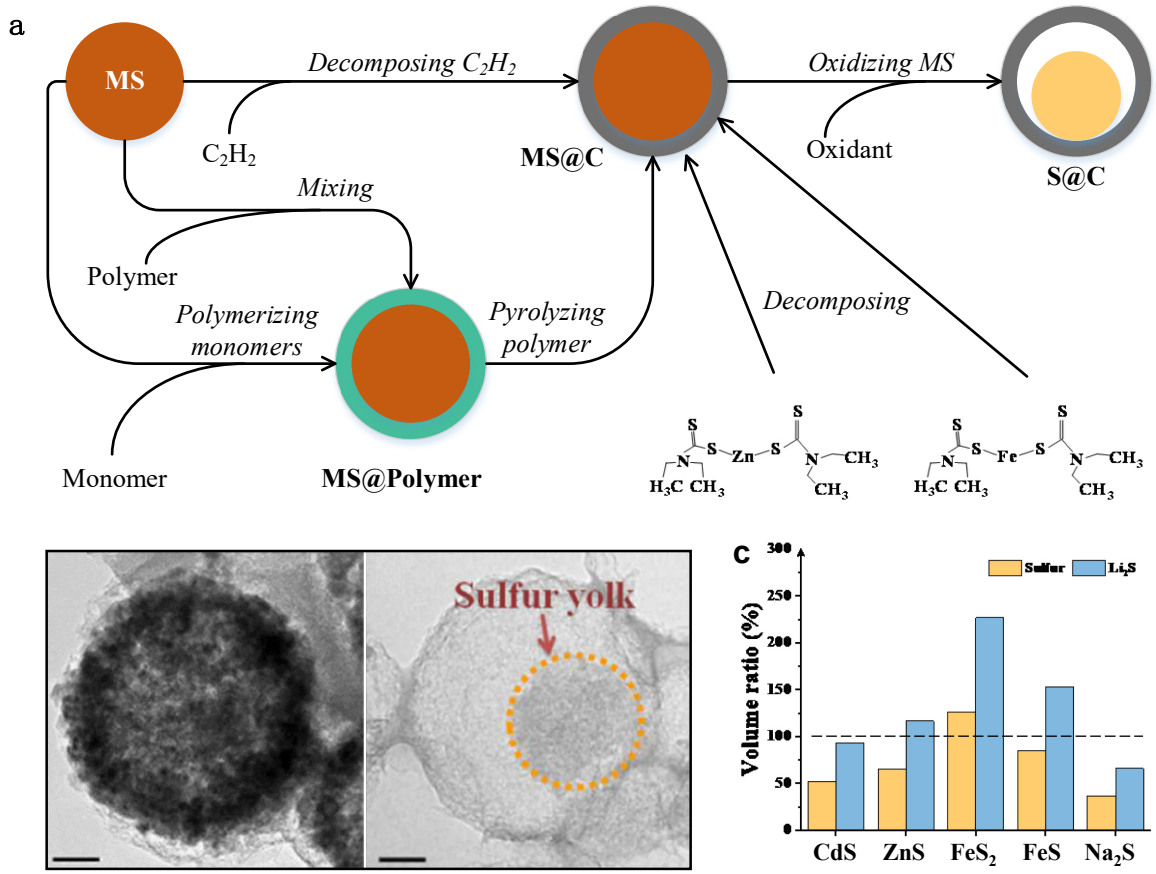

Figure 5. (a) A schematic illustrating fabrication of S@C by reducing metal sulfide or disulfide encapsulated by carbon. (b) SEM images of carbon encapsulated ZnS NP (left) and yolk-shell structured S@C derived from carbon encapsulated ZnS NP (right) [207]. Reproduced with permission from Royal Society of Chemistry. (c) Volume ratio of derived sulfur and Li_2S to metal sulfides.

This carbon encapsulation strategy has clear edges over that presented in Section 2 where sulfur is impregnated into a prefabricated carbon shell. It directly addresses the challenges of the latter on issues of how to fill sulfur into a well-sealed carbon shell without sulfur aggregation on the outer surface. The obtained carbon coated sulfur particles demonstrated much better electrochemical performance thanks to the excellent encapsulation of sulfur

particles into the carbon shell [207]. In addition, this approach can prevent the aggregation of sulfur particles and effectively control uniformity.

Admittedly, this strategy has its own drawbacks. Carbon shell pulverization may occur during the conversion of metal sulfides or metal disulfides to the elemental sulfur in the electrode preparation, and the elemental sulfur conversion to Li_2S during the battery cycling. Based on the molar volume of Li_2S (27.7 cm^3 mol^{-1}), that of the metal sulfide and the disulfide precursor should be higher than 27.7 and 55.4 cm^3 mol^{-1}, respectively, to avoid volume expansion from the precursor to Li_2S. As shown in Figure 5 (c), conversion of certain metal sulfides or disulfides, e.g. FeS_2, to sulfur will experience volume expansion and result in sulfur overflow from the carbon shell, and even worse, the carbon shell fracture. For carbon coated sulfur particles derived from ZnS and FeS, the sulfur volume can be accommodated in the shell, but not for the discharged product of Li_2S. In this sense, CdS and Na_2S is the best precursor, since the derived sulfur and Li_2S both have a volume smaller than the carbon shell, but the remaining void space may lead to a low energy density.

Perhaps, the best sulfide precursor candidate for this encapsulation strategy is Li_2S itself. Like other metal sulfides, Li_2S NPs can be easily encapsulated with a polymer layer, which is then carbonized into a conformal carbon coating [215-217]. The carbon coating can also be implemented via the decomposition of C_2H_2 at a high temperature [218, 219]. Since Li_2S is the discharge product of sulfur, the extra step to oxidize metal sulfide into sulfur is eliminated. And the aforementioned problems of volume expansion or the low energy density automatically disappear. With the cathode fully prelithiated by using Li_2S, Li-free anode could also be used. Issues with Li_2S as the precursor include its sensitivity to water vapor and the large activation

barrier when particle size is large. The pros and cons of using Li_2S as the starting cathode material can be found in a recent review [220].

Different sulfur cathodes prepared with metal sulfide or disulfide as a precursor and their electrochemical performance are summarized in Table 3.

Table 3 Different sulfur cathodes prepared with metal sulfides or disulfides as a precursor and their electrochemical performance.

Metal sulfides	Precursors for carbon	Temperature to obtain carbon coated MS or MS_2 (°C)	Sulfur content (%)	Sulfur loading (mg cm^{-2})	Initial capacity (mAh g^{-1})	Cycling number @ cycling rate	Decay rate (% per cycle)	Ref.
CdS nanospheres	PDA	500	49.8	1.0	179	300 @ 2.0 C	0.035	[203]
ZnS nanosheets	PDA	700	32.6	-	688	200 @ 5.0 C	0.064	[206]
ZnS nanospheres	PDA	800	51.0	1.5	817	500 @ 0.94 C	0.107	[208]
ZnS nanospheres	RF	750	67.5	2.3	1,000	150 @ 0.10 C	0.200	[205]
ZnS nanospheres	PF	900	28.8	0.45	1,493	100 @ 0.23 C	0.370	[207]
ZnS nanosheets	Acetylene	900	48.0	13.3	377	200 @ 0.20 C	-0.300	[204]
Zinc dimethyldithiocarbamate		750	59.2	3.6	988	120 @ 0.10 C	0.028	[211]
FeS_2 NPs	PVP	500	35.0	1.0	800	250 @ 0.50 C	0.170	[209]
iron (II) diethyl dithiocarbamate		750	59.2	3.0	950	280 @ 1.0 C	0.050	[210]
Na_2S crystals	Glucose	750	72.0	2.4	1,115	1,000 @ 2.0 C	0.039	[214]
Li_2S NPs	Acetylene	450	83.6	0.8	1,397	100 @ 0.2 C	0.240	[219]

Li_2S NPs	Acetylene	450	51.0	0.8-0.9	1,427	100 @ 0.2 C	0.240	[221]
Li_2S NPs	PVP	600	67.6	1.7-2.4	656	200 @ 1.0 C	0.080	[222]
Li_2S NPs	PAN	600	51.1	1.0	1,264	200 @ 0.5 C	0.170	[216]
Li_2S NPs	PAN	1,000	46.5	2.1-2.4	1,396	200 @ 0.1 C	0.206	[223]

6. Variations of the core-shell structure

Using the various encapsulated sulfur particles for the cathode, as surveyed in Sections 4 and 5, has dramatically boosted LSB electrochemical performance, but there remains a plenty of room to improve such a NP structure. In this section, we will review the different variations and improvements of the conventional core-shell structures associated with encapsulation methods, which are classified to variations of the core, the shell, and the external connection of these particles.

6.1 Variations of the particle core

As sulfur experiences a volume expansion up to 80% when fully converted to Li_2S during discharge, it is necessary to reserve a buffer space in the core in order to accommodate the volume expansion for maintaining the integrity of the sulfur cathode. In this context, a yolk-shell based sulfur particle structure is better than the conventional core-shell structure. As schematically shown in Figure 6 (a), two methods have been attempted to achieve this variation. As sulfur has a moderate solubility in toluene, dispersion of the core-shell sulfur composite NPs in toluene leads to partial sulfur extraction from the core region while maintaining its shell intact [108, 119, 185]. In contrast, Abruña's group found that when partially leaching sulfur from a S@PANI core-shell structure, the sulfur core was easily dissolved completely and the

PANI shell was subsequently collapsed [113]. Inspired by the discovery that elemental sulfur can react with PANI to form a cross-linked stereo network via inter- and/or intra-chain disulfide bond [224], yolk-shell structured S@PANI was easily achieved through mildly heating its core-shell counterpart [113]. Figure 6 (c) displays the TEM images of the yolk-shell structured S@TiO_2 after partially dissolving sulfur from the core-shell structured S@TiO_2, and the yolk-shell structured S@PANI after heating core-shell structured S@PANI [113, 185]. As the void space in the core is capable of accommodating the volume expansion of sulfur materials during discharge, the yolk-shell structure is well retained after cycling, in comparison with that nearly all spherical morphology has been destroyed for the core-shell structured ones [113, 185], as shown in Figure 6 (d). Thus, the former demonstrated much better performance than the latter, since its intact shell provides a more effectual barrier for the outward diffusion of LiPSs. For instance, the yolk-shell structured S@MnO_2 exhibits a capacity fading rate of 0.040% per cycle during 300 cycles, in comparison with 0.117% for the core-shell structured one [108].

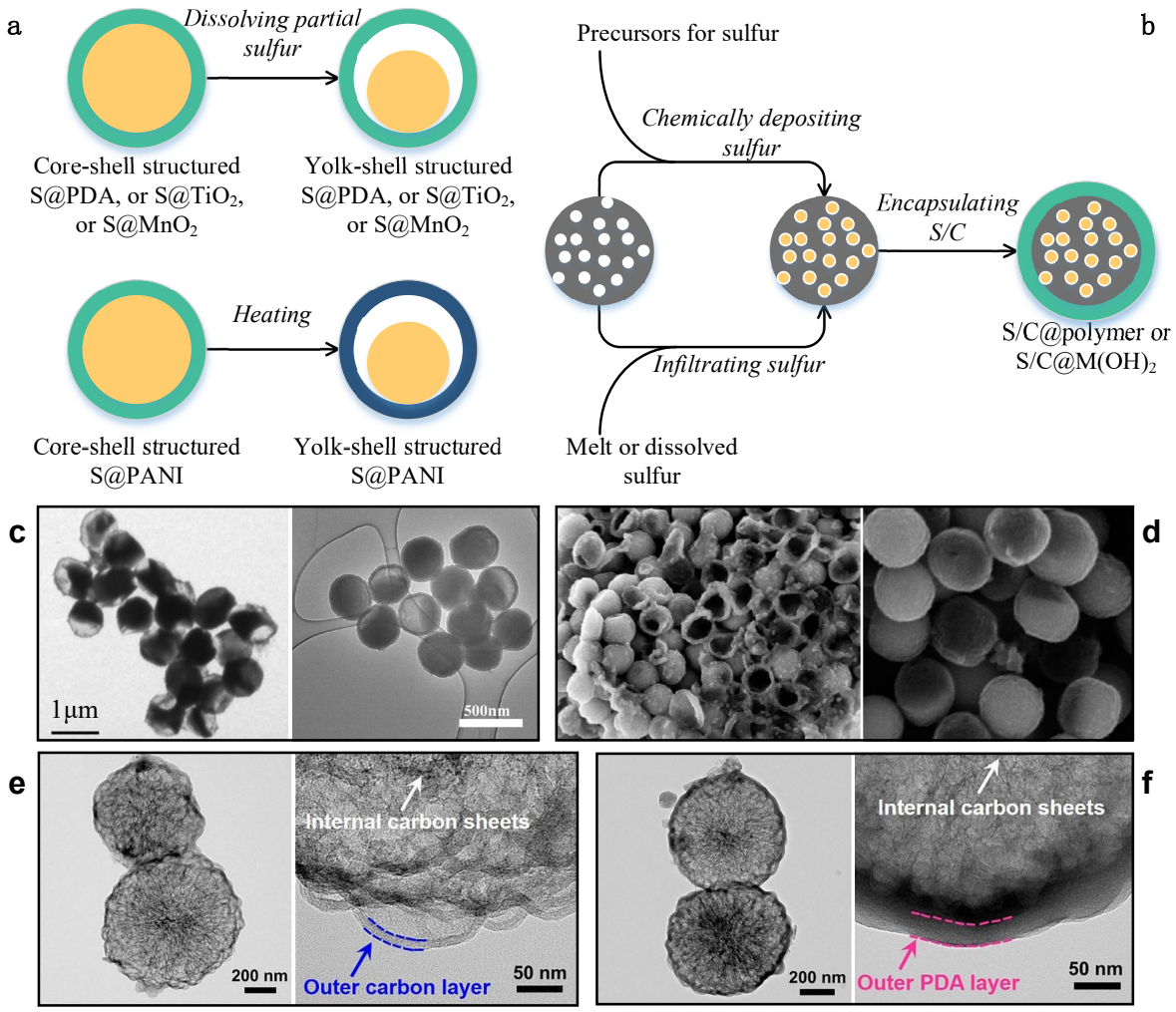

Figure 6. (a) A schematic showing transformation from the core-shell structure to the yolk-shell structure. (b) A schematic showing the compositing process of sulfur and carbon and the subsequent encapsulation process. (c) TEM images of yolk-shell structured S@TiO_2 (left) and S@PANI (right) [113, 185]. Reproduced with permission from Nature Publishing Group and American Chemical Society. (d) SEM images of the core-shell structured and the yolk-shelled S@PANI after 5 cycles [113]. Reproduced with permission from American Chemical Society. TEM images of (e) porous carbon nanospheres and (f) PDA encapsulated porous carbon nanospheres filled with sulfur [136]. Reproduced with permission from Wiley.

Another issue associated with the sulfur core is its poor electronic conductivity, which will largely decrease the utilization of the sulfur species and degenerate the rate performance of the cathode. This is particularly true for the core with a large diameter. After the part of sulfur or Li_2S_2/Li_2S that directly connects with the inner shell is converted to LiPSs and dissolved, the remaining core will detach from the shell and becomes dead material. As we know, sulfur and Li_2S_2/Li_2S detachment from the conductive host is one of the main problematic issues resulting in poor electrochemical performance of LSBs [69]. This detrimental effect may be more severe for a large core.

To attack this problem, composite core structures have been proposed and developed. Specifically, a sulfur/carbon composite is first synthesized based on methods such as by diffusing melted sulfur into the nanopores of carbon where it solidifies [135, 136, 174, 200, 201, 225-229], or recrystallizing [129], or chemically generating sulfur particles inside/on a carbon host [139, 159, 172, 230, 231]. The as-attained sulfur/carbon composite is applied as the core being encapsulated with a polymer or metal hydroxide coating by *in situ* oxidative polymerization of monomers or hydrolysis of transition metal salts, respectively, as schematically shown in Figure 6 (b). Figure 6 (e) and Figure 6 (f) present the TEM images of the porous carbon nanospheres composed of carbon nanosheets, and the PDA encapsulated porous carbon nanospheres composited with sulfur, respectively. The carbon nanosheets in the core, in connection with the shell and/or the outside conductive additives, not only provides a conduit for electron transport, but also serves as redox reaction sites for conversion of sulfur species. When the selected shell material has a poor conductivity, the benefits from the interlaced carbon in the core would become more obvious. In addition, the carbon material also

serves as an additional physical barrier to suppress the outward diffusion of LiPSs. Due to the synergistic effect of the interlaced carbon and the shell, such constructed sulfur cathodes demonstrated enhanced electrochemical performance. For instance, the cathode based on S/carbon black@$Ni_3(NO_3)_2(OH)_4$ exhibited almost 100% Coulombic efficiency and negligible capacity decay within 500 cycles [200].

Following the aforementioned argument, the core-shell structure with a composite core can also be fabricated using the melt-diffusion method after the prefabricated hollow hosts are first modified with CNTs, carbon spheres, or foam-like carbon filler [30, 232, 233]. Besides using carbonaceous materials as a modifier to enhance conductivity for improved sulfur utilization, other materials including MnO_2, Fe_3O_4, NiS_2, have been attempted to modify the hollow structure before impregnating sulfur via melt diffusion [60, 68, 166, 234]. These modifiers, as previously discussed, play roles such as chemical binding to LiPSs and as electrocatalyst promoting the redox kinetics between sulfur species, thus compensating the deficiencies of the carbon shell.

The carbon introduction in the core not only boosts the electrochemical performance of LSBs, but also provides the conditions for using the LBL technique to encapsulate sulfur/carbon. In the LBL deposition, oppositely charged polyelectrolyte layers are assembled to a PEML through electrostatic interactions. After being treated by an acid or alkaline solution, carbon exhibits a negatively charged surface with incorporation of hydrophilic groups (hydroxyl and carboxyl) on its external surface [235-237]. For instance, the Ketjen Blacks® after refluxing in nitric acid showed a zeta potential of -48 mV [170]. As the PEML is assembled by electrostatic interaction, negatively charged carbon is introduced to mix with

sulfur first, and then the sulfur/carbon composite is sequentially encapsulated by oppositely charged polyelectrolytes [170, 171]. Owing to the strong electrostatic interactions between the oppositely charged materials, the PEML membrane is very stable and the coating procedure is facile. When S/carbon@PEML is applied for sulfur cathodes, the PEML membrane shows effectiveness in blocking the polysulfide diffusion and promoting the lithium ion diffusion. Such LBL technique exhibits great flexibility as the thickness and permeability of the PEML membrane could be well tuned by selecting different polyelectrolytes, varying the number of layers and the ionic strength for the PEML membrane formation.

Another simple method to encapsulate a sulfur/carbon composite is mixing it with a polymer, as the latter can easily form a homogeneous and compact surface layer enclosing the sulfur/carbon composite [172-175]. However, the polymer coating is formed around the large sulfur/carbon bulk, rather than each nano-sized unit containing sulfur. So, a nanoscale core-shell structure is not formed, and it is not able to prevent the outward diffusion of LiPSs.

6.2 Variations of the particle shell

A single coating layer on the sulfur particles might not be enough to realize the desirable electrochemical performance due to its deficiency in some respects. For instance, although metallic and carbonaceous materials exhibit superior electronic conductivity, they only provide physical confinement and fall short in eliminating the outward diffusion of LiPSs. In contrast, the transition metal sulfides, oxides, and hydroxides are found to be effective in chemically anchoring LiPSs, and some even serve as electrocatalysts to promote the redox conversion of polysulfides. However, their poor electronic conductivity compromises the rate performance

of such based sulfur cathodes. Regarding the polymers, they generally exhibit a poor wettability with the electrolyte and thereby slow down the redox kinetics. Moreover, for polymer coatings such as that of PPY, due to the presence of large pores (~5 nm), the encapsulating PPY layer exhibits limited effects in ameliorating the shuttle effect and enhancing the electrochemical performance of sulfur cathodes, even though it has a relatively high electronic conductivity [114]. Among the currently studied materials applied for encapsulation, they each have their unique merits but are far from perfect. Accordingly, it is necessary to combine the merits of different host materials together for different functionalities. Thus, a hybrid shell is expected to synergistically boost the electrochemical performance of sulfur cathodes.

In this context, the double-layer shell has been realized by carrying out the encapsulation procedure twice [112, 114], as schematically shown in Figure 7 (a). For instance, sulfur nanospheres are first encapsulated by PPY through the polymerization of pyrrole at room temperature to achieve the core-shell structured S@PPY, and then the interfacial sulfur between the sulfur core and the PPY shell is transformed to MnO_2 via the reaction with $KMnO_4$ [114]. Using a similar two-step encapsulation method, Yan et al. prepared S@PEDOT@MnO_2. Specifically, a PEDOT layer is initially coated on the sulfur nanosphere to achieve S@PEDOT, and then the outer surface of the PEDOT shell is converted to amorphous MnO_2 nanosheets via the redox exchange of permanganate ions with the functional groups on PEDOT [112]. The final shell, composed of both MnO_2 and a conducting polymer (such as PPY and PEDOT), inherits the merits from both MnO_2 and the conducting polymer. PPY and PEDOT not only improve the electronic conductivity of MnO_2, but also increase the mechanical strength of the MnO_2 shell. In addition to its merits as discussed in Section 4.4, the MnO_2 shell enhances the

wettability of the electrode in the electrolyte, and thus promoting the redox kinetics for conversion of sulfur species, as verified by the EIS measurement [112]. Accordingly, the double-layer shell MnO_2@PPY and PEDOT@MnO_2 based structures demonstrate better performance than their individual counterparts of MnO_2, PPY, and PEDOT [112, 114]. The S@PEDOT@MnO_2 NPs deliver an initial specific capacity of 1150 mAh g^{-1} at 0.2 C, and show a low decay rate of 0.140% per cycle, in comparison with 1093 mAh g^{-1} and 0.250% for S@PEDOT [112]. The comparison of self-discharge properties between S@MnO_2@PPY and sulfur nanospheres further indicates that the double-layer shell has a strong ability to restrain the diffusion of LiPSs [114]. After 168 h resting, the LSB based on S@MnO_2@PPY retained 91% capacity, much higher than that based on bare sulfur nanospheres (66%).

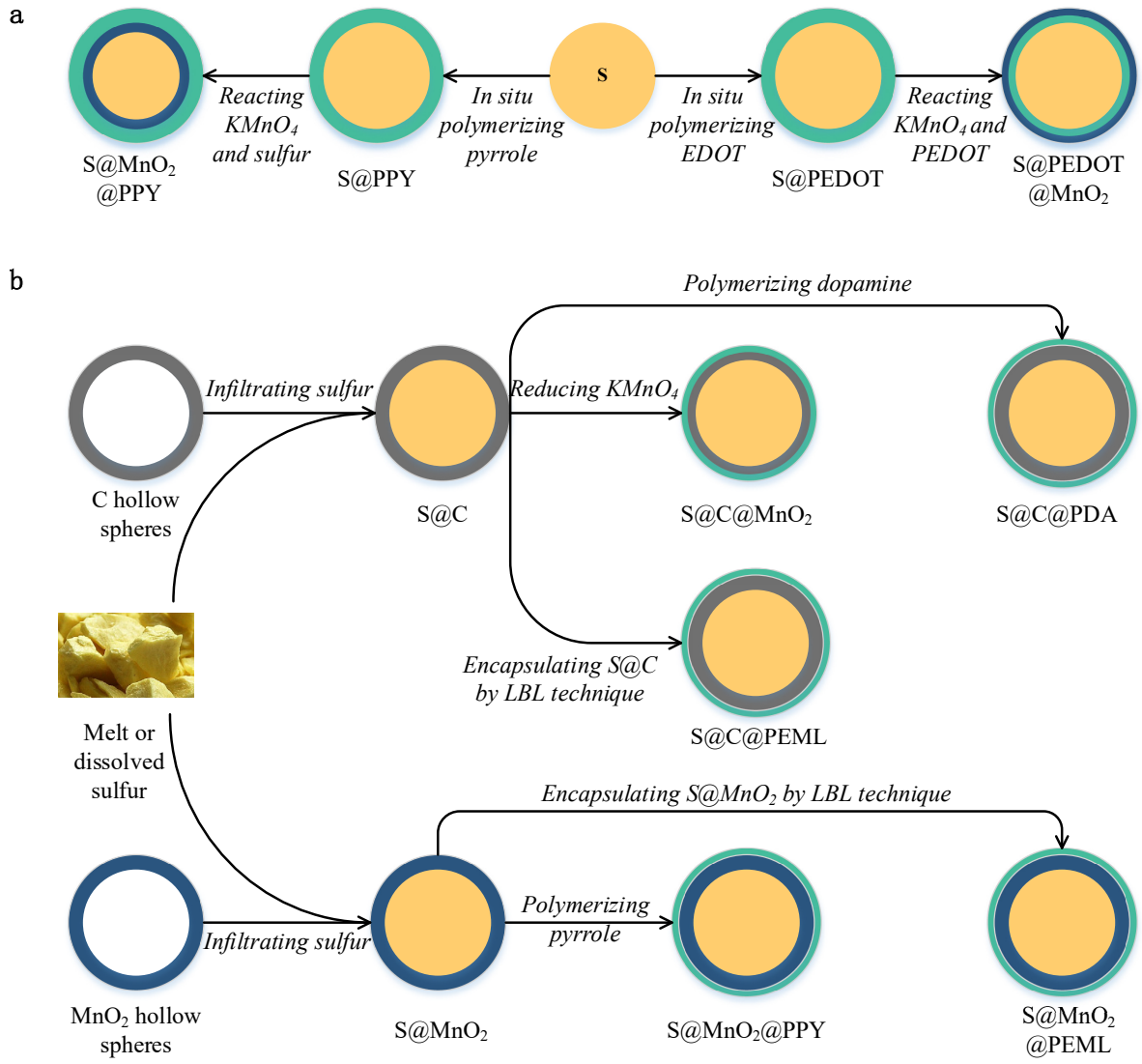

Figure 7. A schematic to illustrate the shell modification process by (a) carrying out encapsulation procedure twice and (b) combining infiltration with encapsulation.

In addition to the two-step encapsulation method, a double-layer shell structure could also be created by combining the infiltration strategy with the encapsulation strategy, as schematically illustrated in Figure 7 (b). The beauty of this combined infiltration-encapsulation approach is that it brings the merits of the two strategies together while discarding their individual weaknesses. As highlighted in Section 2, the infiltration strategy uses the sulfur

powder as the source without bothering the synthesis of sulfur NPs but faces the challenge of low filling efficiency when a tightly sealed hollow structure is used. On the other hand, the encapsulation strategy has no filling issue, but sulfur NPs must be synthesized first. Now in the combined infiltration-encapsulation approach, sulfur powder is directly used to easily fill into a highly porous (leaky) inner-shell, which is then further sealed by a tight outer-shell through encapsulation. In addition, different shell materials can be used to provide multiple functions that are not available from a single component.

For instance, the hollow carbon spheres are first impregnated with sulfur by the melt-diffusion or dissolution-diffusion method to achieve core-shell structured S@C. The S@C is further encapsulated with MnO_2 by reduction of $KMnO_4$ [194], as both sulfur and carbon could serve as the reductant [108, 238], or it can be coated by PDA via dopamine polymerization on its surface [85]. The hollow carbon shells serve as both a dispersing agent to downsize large sulfur particles and an electron transport path to enhance the electronic conductivity of the electrodes, making it feasible to apply commercially available sulfur as the sulfur precursor for encapsulation. The void core space as well as those pores in the carbon shell accommodates the volume expansion during discharge, ensuring the integrity of the electrode. In comparison with its easy sublimation in S@C, sulfur in the S@C@PDA particles could withstand the electron beam heating and the ultra-high vacuum under STEM characterization [85]. Thus, it is reasonable to consider that the double-layer shell serves as a more effective barrier to the outward diffusion of LiPSs. Due to the synergistic effect of the carbon shell and the PDA shell, the S@C@PDA based cathode exhibited extraordinary electrochemical performance of an initial specific capacity of 1141 mAh g^{-1} at 0.2 C and a fading rate of 0.107% per cycle during

150 cycle, in comparison with 1070 mAh g^{-1} and 0.322% for S@C based one. LBL technique has also been applied to encapsulate core-shell structured S@C that achieved via melt diffusion. The synthesized S@C@PEML exhibited enhanced electrochemical performance in comparison with S@C [235].

Besides carbon hollow spheres, sulfur could also be filled into MnO_2 hollow spheres by the melt-dissolution or the dissolution-diffusion method first and then further wrapped using an encapsulation method [239, 240]. Benefiting from the dual shell structure, S@MnO_2@PPY based cathode retained a specific capacity of 704 mAh g^{-1} after 500 cycles at 0.5 C, showing an average capacity decay rate of only 0.048% per cycle.

To sum up, the multi-layer shell engineering provides possibility to further enhance the electrochemical performance of the sulfur cathode by offering a multifunctional and possibly a well-sealed shell. Downsizing commercially available sulfur powder into a leaky shell by the infiltration strategy would cut the cost and simplify the encapsulation process.

6.3 Interconnection between particles

Although encapsulating sulfur NPs is effective in inhibiting the shuttling of LiPSs, many of the coating materials have poor electronic conductivity, which may lead to sluggish redox reactions. The monodispersity of the encapsulated sulfur NPs as spheres limits the contact area between each other, which further hampers electron transport across NPs. During the charge/discharge process, the volume change of the electrode would make this problematic issue worse. Therefore, it is necessary to create interconnected conductive networks between the encapsulated sulfur NPs, as schematically shown in Figure 8.

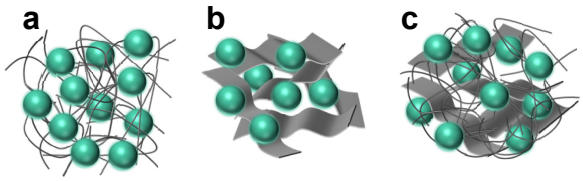

Figure 8. A schematic to illustrate the interconnection between encapsulated sulfur NPs based on (a) CNTs, (b) RGO or GO, and (c) RGO or GO and CNTs.

Due to their superior electronic conductivity and excellent mechanical flexibility, CNTs were applied to interconnect with S@PEDOT [124]. The introduced CNTs not only facilitate electron transport, but also reinforce the mechanical strength of the sulfur cathode. The latter effect helps maintaining the integrity of the electrode during charge/discharge. Moreover, a flexible and binder-free electrode can be fabricated by ultrasonically mixing S@PEDOT and CNTs and then filtrating the mixture. The absence of adhesive agent increases the sulfur content of the electrode and enhances its electronic conductivity.

Graphene oxide (GO) and reduced graphene oxide (RGO) or graphene are another two materials to connect the encapsulated sulfur NPs. Their sheet morphology helps reduce the internal resistance of the electrode by changing electron transport from a “point-to-point” mode to a more effective “plane-to-point” mode [235]. Due to the superior dispersibility of GO in water, the composite of S@MnO_2 and GO was simply achieved by dispersing S@MnO_2 into the GO suspension and centrifuging the mixture [241]. The introduction of GO largely compensates the poor electronic conductivity of MnO_2. In addition, the abundant functional groups located on the surface of GO can adsorb the LiPSs via chemical interaction, thereby alleviating the shuttle effect. The reports by Zhang et al. and Wu et al. revealed that the

electrostatic interactions between the negatively charged GO and the positively charged encapsulating layer made their combination more stable [158, 235].

To balance the electronic conductivity and the chemical binding, GO mixed with S@PPY and S@SiO_2 was partly reduced [122, 186]. The network constructed by RGO serves as a three-dimensional electron transport path, while the remaining oxygen-containing functional groups in RGO provides chemically anchoring sites for LiPSs, both of which contribute to the enhanced electrochemical performance of S@PPY/RGO and S@SiO_2/RGO. Graphene and carbon nanotubes were also collectively used to create interconnected conductive networks, so as to facilitate the electron transfer in three dimensions [164].

Although numerous materials have been developed to encapsulate sulfur NPs, the materials introduced to composite with encapsulated sulfur NPs are limited to CNT, GO, and RGO. More efforts are needed to develop promising candidates. It is worth noting that their introduction may lead to a lower sulfur content.

Derivatives from the conventional core-shell structure and their corresponding electrochemical performance are summarized in Table 4.

Table 4 Derivatives from the conventional core-shell structure and their corresponding electrochemical performance.

Core	Shell	Interconnection	Sulfur content (%)	Sulfur loading (mg cm^{-2})	Initial specific capacity (mAh g^{-1})	Cycling number @ cycling rate	Decay rate	Ref.
Sulfur yolk	PANI	W/O	46.4	2.0	1,039	200 @ 0.20 C	0.150	[113]
Sulfur yolk	PDA	W/O	78.8	0.5-0.6	713	400 @ 0.50 C	0.115	[119]
Sulfur yolk	TiO_2	W/O	53.0	0.4-0.6	1,030	1000 @ 0.50 C	0.033	[185]
Sulfur yolk	MnO_2	W/O	64.0	4.1	1,000	200 @ 0.20 C	0.200	[108]
Sulfur yolk	MnO_2	W/O	21.6	1.6	1,307	100 @ 0.10 C	0.330	[241]

Sulfur/CNT	PANI	W/O	45.5	-	1,225	400 @ 0.25 C	0.095	[139]
Sulfur/ carbon black	PANI	W/O	30.6	1.5-2.0	1,406	100 @ 1.0 C	0.576	[225]
Sulfur/ carbon fiber	PEDOT	W/O	56.6	5.0	760	50 @ 0.10 C	0.800	[172]
Sulfur/ graphene	PEDOT	W/O	52.6	1.0	1,198	200 @ 0.10 C	0.148	[174]
Sulfur/ carbon black	PDA	W/O	41.6	1.2-1.5	1,185	200 @ 0.20 C	0.093	[135]
Sulfur/carbon nanosphere	PDA	W/O	45.5	1.0	1,331	200 @ 0.50 C	0.300	[136]
Sulfur/ carbon black	$Co(OH)_2$	W/O	41.5	-	829	200 @ 1.0 C	0.153	[228]
Sulfur/CNT	$Ni(OH)_2$	W/O	63.0	3.0	720	500 @ 1.0 C	0.061	[201]
Sulfur/ carbon black	$Ni(OH)_2$	W/O	47.2	1.5	897	100 @ 0.20 C	0.199	[229]
Sulfur/ carbon cloth	$Ni_3(NO_3)_2(OH)_4$	W/O	29.7	4.3	838	350 @ 0.50 C	0.064	[129]
Sulfur/ carbon black	$Ni_3(NO_3)_2(OH)_4$	W/O	62.4	1.8-2.5	968	500 @ 0.2 C	-0.058	[200]
Sulfur core	MnO_2@PPY	W/O	66.0	2.5	1,050	135 @ 1.0 C	0.132	[114]
Sulfur core	PEDOT@MnO_2	W/O	65.3	-	1,150	200 @ 0.2 C	0.140	[112]
Melt-diffused sulfur	Carbon@MnO_2	W/O	40.7	3.0	983	500 @ 1.0 C	0.088	[194]
Melt-diffused sulfur	Carbon@PDA	W/O	55.0	1.5	1,070	150 @ 0.2 C	0.107	[85]
Melt-diffused sulfur	MnO_2@PPY	W/O	59.4	3.3	1,372	200 @ 0.15 C	0.149	[239]
Melt-diffused sulfur	MnO_2@PEML	W/O	52.5	0.8	701	300 @ 0.1 C	0.067	[240]
Sulfur core	PEDOT	CNT	58.0	1.5-2.0	700	250 @ 0.5 C	0.096	[124]
Sulfur core	PANI	GO	54.7	1.8-3.0	1,485	100 @ 0.2 C	0.508	[158]
Sulfur yolk	MnO_2	GO	17.6	1.6	1,597	100 @ 0.1 C	0.22	[241]
Sulfur core	SiO_2	RGO	54.0	-	1,150	50 @ 0.1 C	0.678	[186]
Sulfur core	PPY	Graphene	29.4	0.7-0.9	895	200 @ 0.5 C	0.208	[122]
Melt-diffused sulfur	Carbon@PEML	Graphene	52.0	1.7-2.1	820	200 @ 0.6 C	0.149	[235]
Sulfur core	$Ni(OH)_2$	RGO& CNT	59.6	1.5	956	250 @ 0.2 C	0.179	[164]
Sulfur core	NiCo-DH	RGO& CNT	59.6	1.5	1,132	250 @ 0.2 C	0.057	[164]

7. Sulfur encapsulation for aqueous batteries

This article has been mainly focused on reviewing studies of sulfur particle encapsulation

for the sulfur cathode in a conventional LSB that uses an organic ether-based electrolyte. However, notable progress is being made recently in studies of aqueous batteries that contain a sulfur cathode or a sulfur anode [242-244]. Without using organic solvents, aqueous batteries offer their unique properties, including significant benefits in terms of safety, environmental friendliness, and low cost. An aqueous electrolyte further provides an ionic conductivity of approximately two orders of magnitude higher than that of an organic electrolyte, which makes it possible to develop high-power batteries. Motivated by recent progress, research on aqueous batteries is gaining attraction. Therefore, as an extension of this review, we here briefly summarize the progress made when applying encapsulated sulfur in an aqueous electrolyte battery chemistry.

In the case of using sulfur as the cathode material, the configuration of two compartment cell is applied to enable the use of an aqueous electrolyte at the sulfur cathode and an organic electrolyte at the lithium metal anode [245]. And in fact this kind of battery is an aqueous-organic hybrid one. In the case of sulfur applied as an anode, an all-aqueous system has been explored by pairing the sulfur anode with a lithium intercalation cathode [246, 247].

It is worth noting that the redox electrochemistry of sulfur in aqueous electrolytes is different from that in organic electrolytes. In aqueous electrolytes, three main chemical species are formed during sulfur reduction, including H_2S(aq.), HS^-, and S_x^{2-}, rather than Li_2S_x and Li_2S_2/Li_2S [141, 248]. Similar to that in organic electrolytes, the dissolution and diffusion of H_2S(aq.), HS^-, and S_x^{2-} in aqueous electrolytes would result in inferior electrochemical performance. A PPy layer encapsulating on the sulfur particles can restrain sulfur species from diffusing into the electrolyte, and consequently the redox reaction of sulfur is highly reversible

and stable [141, 248].

Yang et al. found that sulfur electrode in water-in-bisalt electrolytes (WiBS) followed a similar lithiation pathway to that in organic electrolyte, represented by the formation of Li_2S_6, Li_2S_4, Li_2S_2, and Li_2S [249]. The absence of H_2S(aq.), HS^-, and S_x^{2-} could be attributed to that the hydrolysis of Li_2S_x is effectively suppressed in the WiBS electrolyte system because of the low activity of water molecules that are tightly bound by the abundant cations and anions. Under this circumstance, the artificial confinement of Li_2S_x and Li_2S_2/Li_2S is not imperative, as they are effectively expelled from the WiBS electrolyte by an extremely high concentration of lithium salts [249]. Nevertheless, an encapsulating layer on sulfur particles is expected to provide electron transport paths or serve as electrocatalysts in the electrode, thereby improving its performance.

It is worth to emphasize that aqueous electrolytes themselves do not directly address the problem of low sulfur utilization and sulfur species shuttling since the sulfur species still dissolve and diffuse in the aqueous electrolyte. Therefore, sulfur particle encapsulation is still necessary to improve the sulfur utilization and electrochemical performance of the battery. More studies of encapsulated sulfur are expected to be conducted in the aqueous electrochemistry.

8. Summary and future works

8.1 Summary

The core-shell sulfur composite NPs exhibit a multitude of merits when applied for the sulfur cathode. Although these structured NPs could be easily produced following the

infiltration strategy via melt-diffusion, dissolution-diffusion, or vapor-phase infusion, their quality is generally low as a result of contradictory requirements in term of easy infiltration and tight sealing. Encapsulation, therefore, has emerged as an alternative strategy to fabricate the core-shell structured sulfur composite NPs.

In the encapsulation strategy, the prefabricated sulfur NPs are conformally encapsulated by a shell. Sulfur NPs have been synthesized by either reacting $Na_2S_2O_3$ with acid under the guidance of PVP or other surfactant micelles or using elemental sulfur as the precursor in a guided recrystallization process or a controlled chemical process.

The low melting point of the sulfur core restrains the shell encapsulation to be performed at or close to room temperature, and self-assembling around the sulfur core in a solution (or in its liquid state in the case of a metal shell) becomes the natural choice. Five categories of materials—polymers, metals, sulfides, oxides, and hydroxides— have all been attempted to form the shell. These encapsulating materials each demonstrate their strengths and weaknesses in terms of electronic and ionic conductivity, physical confinement and chemical binding of LiPSs, specific surface area, and electrocatalytic function, etc.

Different from that of sulfur NP itself as the starting core, metal sulfide or disulfide NPs could also be used, which are converted into elemental sulfur after encapsulation. This approach overcomes the low-temperature restraints exerted by a sulfur core, and hence high-temperature processes of shell coating, particularly those of carbon coating now can be adopted. The carbon encapsulated sulfide or disulfide NPs are then converted to core-shell or yolk-shell sulfur@carbon nanostructures.

To further enhance their electrochemical performance, the conventional core-shell structure

can be further modified by changing the core composition, engineering the multilayered and multifunctional shell, and the interconnections between the encapsulated NPs. In particular, the combined infiltration-encapsulation approach for the bilayer shell engineering merges the merits of the two strategies together while discarding individual's weaknesses, providing a better strategy with a potential for large-scale production of encapsulated sulfur NPs.

Not only encapsulation strategies can enhance the electrochemical performance of sulfur cathodes working in ether-based electrolytes, can they boost that of sulfur electrodes working in aqueous electrolytes, as the batteries based on both ether-based and aqueous electrolytes face similar problems such as poor electronic conductivity of sulfur and high dissolution and diffusion of sulfur species.

8.2 Comments on encapsulation

Although great progress has been made on encapsulated sulfur NPs for the LSB, we feel some critical issues on sulfur encapsulation, in fact, have not been really solved.

Using advanced microscopic imaging techniques, as shown in Figure 3, it is revealed that sulfur particles can be physically encapsulated by a shell using some encapsulation methods. However, whether Li_2S_x intermediates have been perfectly confined in this physically tight shell without out-diffusion is still in question. The effectiveness of Li_2S_x entrapment in the shell has most often been indirectly testified. For instance, DFT calculation, XPS characterization, and adsorption measurements were usually applied to show the chemical binding between Li_2S_x and the shell materials [111, 118, 163]. The interception of Li_2S_x by the shell was also demonstrated by the obvious difference in electrochemical performance in terms of specific capacity, cycling stability, Coulombic efficiency and shuttle current between the bare sulfur

particles and encapsulated sulfur particles [112, 113, 132, 155, 161]. These, however, all are indirect evidences. Furthermore, in most studies, additives such as $LiNO_3$ are used which stop the polysulfide shuttle to show a better battery performance. This suggests that polysulfides might still dissolve and diffuse in the electrolyte.

There have been no studies that directly confirm Li_2S_x are entrapped in the shell. In the reports available, the encapsulated sulfur particles demonstrated a charge/discharge profile with two plateaus, implying they undergo a solid-liquid-solid redox reaction [116, 162, 181]. This means that the encapsulating shell is permeable to the solvent, which may also permit the traverse of Li_2S_x. In view of this, in-situ tools and post-mortem studies are advised to directly observe Li_2S_x confinement resulting from the encapsulation. Especially, electrolytes without $LiNO_3$ and other additives may be a touchstone for testing the encapsulation effectiveness, as without additives, the shuttle effect would become much severer if Li_2S_x are not well confined [250]. Carbonate-based electrolyte is another possible touchstone for this purpose. As we know, sulfur cathodes are incompatible with carbonate-based electrolytes since the nucleophilic Li_2S_x intermediates tend to react with the electrophilic carbonate-based solvents through a nucleophilic addition or substitution reaction, resulting in rapid capacity decay of LSBs [251-253]. Only when the sulfur particles are perfectly confined, can the LSB operates well in the carbonate-based electrolyte.

Then, the question arises: is it feasible to completely entrap Li_2S_x? To answer this question, we must be clear on the constraint when designing the sulfur cathode. Since sulfur and Li_2S_2/Li_2S are highly insulating for both electron and Li^+ transport, it is generally accepted that the cathode reaction should take the solid-liquid-solid path: solid sulfur is in direct contact with

the liquid electrolyte so that initial formed polysulfides are dissolved in the electrolyte to expose fresh sulfur for continuing the reaction, while the dissolved polysulfides, which are confined in the cathode structure, can quickly diffuse back to the electrode surface to further convert into solid Li_2S_2/Li_2S [254, 255].

If this solid-liquid-solid reaction path is still to follow, the encapsulation shell of sulfur particles must allow the electrolyte solvent molecules to diffuse into the shell but shut off Li_2S_x molecules from crossing the shell barrier. As the solvent and the solvated Li_2S_x molecules present a similar size of 0.3−0.8 nm and 1.2−1.7 nm, respectively [118, 255, 256], a dilemma exists to design the shell pore size to achieve rapid transport for electrolytes as well as shutting down the Li_2S_x crossover. Therefore, most often a leaky shell is used with pores that allow for the penetration of the electrolyte into the particles, while solvated polysulfides can more or less also diffuse out of the shell, as shown in Figure 9 (a). Such a design could enhance the confinement of Li_2S_x in the cathode, but impossible to eliminate their shuttling between the two electrodes. This shell will result in improved but diminishing performance.

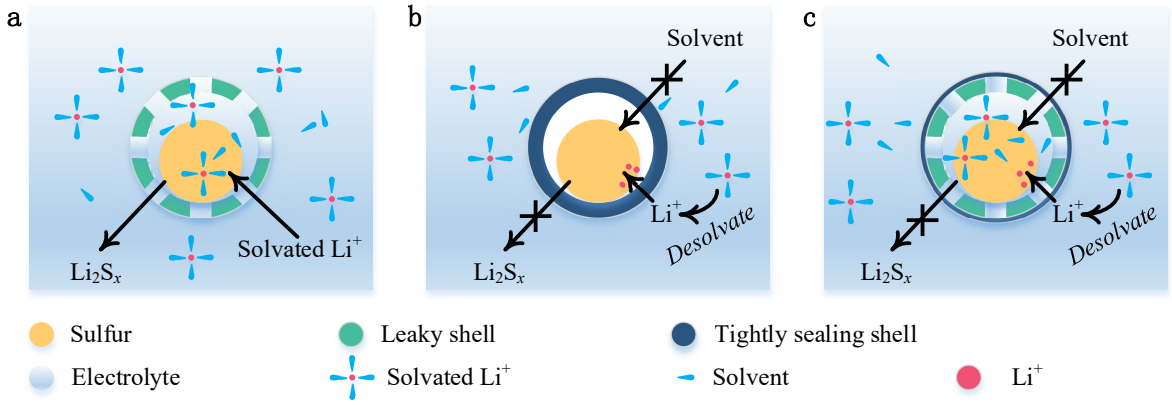

Figure 9. A schematic to illustrate the sulfur particles encapsulated by three different shells. The sulfur particle is encapsulated by (a) a leaky shell and (b) a tightly sealing shell,

respectively. (c) The sulfur particle initially encapsulated by a leaky shell is mixed with the electrolyte first and then encapsulated with a second tightly sealing shell.

On the other hand, since sulfur core-shell NPs are used, we could question if the constraint of the solid-liquid-solid reaction path is still necessary to follow. The nanoscale particle size and a conductive shell might be enough to ensure a reasonable solid-solid reaction kinetics without the mediation of the dissolved liquid phase. For such a scenario, the shell can be tightly sealed eliminating the diffusion of both Li_2S_x and solvents across the particle shell, although it should still allow Li^+ to freely cross over, as shown in Figure 9 (b). Although in several reports [257-259], the filled sulfur in porous carbon through melt-diffusion method demonstrated a solid-solid conversion during discharging in carbonate-based electrolytes, no reports are available on encapsulated sulfur particles showing the same reaction process. Besides, the reason why and how this conversion occurs is still under debate and need further investigation [251, 257, 260].

A third but more attractive strategy is to combine the merits of aforementioned approaches, that is, the leaky NPs is mixed with the electrolyte and then the leaky NPs are coated with a second tightly sealing shell, as shown in Figure 9 (c). Such a dual encapsulation strategy is recently tested by Chen's group using an in-situ re-encapsulation method after cell assembling [255, 261]. Sulfur/carbon composite particles encapsulated with an imperfect layer is assembled into coin cells. The imperfect layer allows the infiltration of electrolyte into the composite particles. A special additive initially added to the electrolyte will react with the imperfect layer to form a second coating layer after the battery is assembled. The second

coating layer is designed to be compact and tight to completely retain the Li_2S_x. This delicate encapsulating method endows the cell with a capacity decay as small as 0.03% per cycle under 1 C during 1000 cycles [255]. It should be emphasized that in this study, whether the second shell is perfectly sealed is still in question.

8.3 Proposed future work

There is still plenty of work to do in order to further boost the sulfur cathode performance and accelerate the development of a practical LSB technology. We consider followings are some research opportunities that deserve to be pursued:

1) Actual evidences of effective encapsulation when used in the battery cells have seldom been reported. Direct proofs on the entrapment of Li_2S_x by the shell are suggested to be provided through in-situ or post-mortem studies or by using electrolytes without nitrate additive or even carbonate-based electrolytes.

2) Whether the solid-solid reaction is feasible in encapsulated sulfur NPs needs to be addressed. If it is feasible, then a tightly sealed shell should be pursued. Otherwise, methods to tightly seal the mixture of sulfur and electrolyte together should be developed to eliminate Li_2S_x shuttling.

3) The mechanism of sulfur infiltration into hollow structures and nanopores should be clearly revealed via *in-situ* observation and theoretical modeling. The current knowledge on this subject is murky and the explanations are plausible. For instance, the capillary action has always been cited to describe the infiltration filling in a melt-diffusion or dissolution-diffusion process; however, the capillary action can only drive the sulfur molecules into the small pores in the shell wall of a hollow structure, and how these molecules further enter into the much

larger hollow space have not been well addressed in the literature. Achieving such fundamental understanding will provide guidelines for the shell structure design and the infiltration process design, so that enough sulfur material can be easily filled into the hollow space while being tightly protected after infiltration.

4) Sulfur NPs with a much small size like SQDs, after proper encapsulation, offer the opportunity to study their much-small-size effect on the sulfur cathode electrochemical performance. Considering the sulfur cathode works as a reactive electrode at its atomic level, in contrast to the intercalation chemistry at the crystal level, the much smaller SQDs might be a promising candidate to overcome the sluggish reaction kinetics in LSBs. It is to be envisioned that the encapsulated much smaller sulfur NPs would prevent the formation of large Li_2S chunks and achieve close to 100% utilization of sulfur atoms. However, the problem of the low yield in SQD synthesis should be solved or other methods to produce much small sulfur NPs should be developed.

5) When oxides, sulfides, hydroxides, and other compounds are used as the encapsulating material, their redox potentials have been largely neglected. As a matter of fact, only when their redox potentials (vs Li^+/Li) range from 2.4 to 3.05 V, can they promote the redox reaction between electrochemically active sulfur species while inhibiting LiPSs from shuttling.

6) When metal sulfides or disulfides are chosen as the sulfur precursor to be encapsulated, the volume change from the metal sulfide or disulfide to sulfur and Li_2S should be taken into account. This includes the possible volume expansion that causes the carbon shell pulverization and volume compression resulting in a low energy density.

7) Li_2S might be the best candidate for encapsulation. The low melting point of sulfur

restrains its encapsulation to a low-temperature process, which excludes the applicability of a conformal and tightly sealed carbon coating. Like other metal sulfides with high temperature processing capability, Li_2S NPs can be easily encapsulated with a polymer layer in a solution, which is then carbonized into a conformal carbon coating. The encapsulation can also be implemented by decomposition of gas-phase hydrocarbon sources at high temperatures. Unlike other metal sulfide precursors, since Li_2S is the discharge product of sulfur, the step to oxidize metal sulfide into sulfur is eliminated. And the problems of volume expansion or the low energy density does not exist.

8) Each encapsulating material has its pros and cons. Further performance enhancement might require a hybrid shell or multilayer shell that offers multiple roles in the sulfur redox process, such as physical trapping LiPSs, chemical binding LiPSs, enhancing electronic or ionic conductivity, and accelerating redox reactions. Overall, the best encapsulating material seems still to be carbon, but it should be assisted by other components.

9) For industrial application, three aspects should be evaluated in terms of performance, running cost, and operation flexibility. The combined infiltration-encapsulation process seems to be a very promising strategy. The low-cost sulfur powder can be directly used as the sulfur source without further processing into NPs, while tightly sealing can also be attained via a facile encapsulation process at room temperature. In addition, The host material in the core and the encapsulating layer could synergistically enhance the electrochemical performance of sulfur cathodes.

10) For a practical LSB technology to challenge the state-of-the-art LIBs, a high sulfur content ($> \sim 75\%$) and a large sulfur mass loading ($> \sim 5$ mg cm^{-2}) in the cathode is needed.

However, the majority of works on sulfur NP encapsulation reported a cathode with much smaller sulfur content and sulfur loading. Future works must balance the amount of encapsulation material used for well protection and the amount of sulfur encapsulated for a large capacity. The sulfur cathode nanostructure should also be carefully designed to minimize the amount of electrolyte used while achieving a high sulfur utilization.

Acknowledgements

S.L appreciates Zhejiang Provincial Natural Science Foundation of China for providing financial support (Grant No. LY19E020011). Z.F acknowledges support from National Science Foundation (1931737) of U.S.A for the work at Texas Tech University.

References

1. L. Zhang, T. Qian, X.Y. Zhu, Z.L. Hu, M.F. Wang, L.Y. Zhang, T. Jiang, J.H. Tian, C.L. Yan, Chem. Soc. 48 (2019) 5432-5453.
2. X. Li, L.X. Yuan, D.Z. Liu, Z. Li, J. Chen, K. Yuan, J.W. Xiang, Y.H. Huang, Energy Stor. Mater. 26 (2020) 570-576.
3. Q. Pang, C.Y. Kwok, D. Kundu, X. Liang, L.F. Nazar, Joule 3 (2019) 136-148
4. A. Manthiram, Y. Fu, S.H. Chung, C. Zu, Y.S. Su, Chem. Rev. 114 (2014) 11751-11787.
5. Z.W. Seh, Y. Sun, Q. Zhang, Y. Cui, Chem. Soc. Rev. 45 (2016) 5605-5634.
6. G. Li, Z. Chen, J. Lu, Chem 4 (2018) 3-7.
7. B. Liu, R.Y. Fang, D. Xie, W.K. Zhang, H. Huang, Y. Xia, X.L. Wang, X.H. Xia, J.P. Tu, Energy Environ. Mater. 1 (2018) 196-208.

8. L. Qie, A. Manthiram, ACS Energy Lett. 1 (2016) 46-51.

9. J.Y. Hwang, H.M. Kim, S. Shin, Y.K. Sun, Adv. Funct. Mater. 28 (2018) 1704294.

10. J. Zhang, Y. Shi, Y. Ding, L.L. Peng, W.K. Zhang, G.H. Yu, Adv. Energy Mater. 7 (2017) 1602876.

11. L. Kong, J.X. Chen, H.J. Peng, J.Q. Huang, W. Zhu, Q. Jin, B.Q. Li, X.T. Zhang, Q. Zhang, Energy Environ. Sci. 12 (2019) 2976-2982.

12. X. Ji, K. T. Lee, L.F. Nazar, Nat. Mater. 8 (2009) 500.

13. S.Q. Li, T. Mou, G.F. Ren, J. Warzywoda, Z.D. Wei, B. Wang, Z.Y. Fan, J. Mater. Chem. A 5 (2017) 1650-1657.

14. S.Q. Li, J. Warzywoda, W. Shu, G.F. Ren, Z.Y. Fan, Carbon 124 (2017) 212-218.

15. L.B. Xing, K. Xi, Q. Li, Z. Su, C. Lai, X. Zhao, R.V. Kumar, J. Power Sources 303 (2016) 22-28.

16. X. Gu, C.J. Tong, S. Rehman, L.M. Liu, Y. Hou, S. Zhang, ACS Appl. Mater. Interfaces 8 (2016) 15991-16001.

17. J. Pu, Z. Shen, J.X. Zheng, W.L. Wu, C. Zhu, Q.W. Zhou, H.G. Zhang, F. Pan, Nano Energy 37 (2017) 7-14.

18. Y. Boyjoo, H. Shi, E. Olsson, Q. Cai, Z.S. Wu, J. Liu, G.Q. Lu, Adv. Energy Mater. 10 (2020) 2000651.

19. Y. Tian, H.W. Huang, G. Liu, R. Bi, L. Zhang, Chem. Commun. 55 (2019) 3243-3246.

20. B.D. McCloskey, J. Phys. Chem. Lett. 6 (2015) 4581-4588.

21. J. Lochala, D.Y. Liu, B.B. Wu, C. Robinson, J. Xiao, ACS Appl. Mater. Interfaces 9 (2017) 24407-24421.

22. T.O. Ely, D. Kamzabek, D. Chakraborty, M.F. Doherty, ACS Appl. Energy Mater. 1 (2018) 1783-1814.

23. H.J. Peng, J.Q. Huang, X.B. Cheng, Q. Zhang, Adv. Energy Mater. 7 (2017) 1700260.

24. Z. Li, H.B. Wu, X.W. Lou, Energy Environ. Sci. 9 (2016) 3061-3070.

25. S. Ma, L. Wang, Y. Wang, P. Zuo, G. Yin, Carbon, 143 (2018) 878-889.

26. R. Pongilat, K. Nallathamby, ACS Appl. Mater. Interfaces 10 (2018) 38853-38861.

27. F. Wang, X. Ding, R. Shi, M. Li, J. Sun, J. Mater. Chem. A 7 (2019) 10494-10504.

28. H. Li, L. Sun, Y. Zhao, T. Tan, Y. Zhang, Electrochim. Acta 295 (2019) 822-828.

29. Y. Zhang, X. Zong, L. Zhan, X. Yu, J. Gao, C. Xun, P. Li, Y. Wang, Electrochim. Acta 284 (2018) 89-97.

30. J. Zang, T. An, Y. Dong, X. Fang, M.S. Zheng, Q. Dong, N. Zheng, Nano Res. 8 (2015) 2663-2675.

31. S.K. Liu, X.B. Hong, D.Q. Wang, Y.J. Li, J. Xu, C.M. Zheng, K. Xie, Electrochim. Acta 279 (2018) 10-18.

32. Y.P. Xie, L. Fang, H.W. Cheng, C.J. Hu, H.B. Zhao, J.Q. Xu, J.H. Fang, X.G. Lu, J.J. Zhang, J. Mater. Chem. A 4 (2016) 15612-15620.

33. J. Hou, X. Tu, X. Wu, M. Shen, X. Wang, C. Wang, C. Cao, H. Pang, G. Wang, Chem. Eng. J. 401 (2020) 126141.

34. S. Chen, B. Sun, X. Xie, A.K. Mondal, X. Huang, G. Wang, Nano Energy 16 (2015) 268-280.

35. S. Chen, X. Huang, H. Liu, B. Sun, W. Yeoh, K. Li, J. Zhang, G. Wang, Adv. Energy Mater. 4 (2014) 1301761.

36. O. Ogoke, S. Hwang, B. Hultman, M. Chen, S. Karakalos, Y. He, A. Ramsey, D. Su, P. Alexandridis, G. Wu, J. Mater. Chem. 7 (2019) 13389-13399.

37. F.Y. Jin, S. Xiao, L.J. Lu, Y. Wang, Nano Lett. 16 (2016) 440-447.

38. Y. Song, H. Wang, Q.L. Ma, D. Li, W.S. Yu, G.X. Liu, T.T. Wang, Y. Yang, X.T. Dong, J.X. Wang,

ACS Sustain. Chem. Eng. 7 (2019) 3042-3051.

39. B.Q. Li, S.Y. Zhang, L. Kong, H.J. Peng, Q. Zhang, Adv. Mater. 30 (2018) 1707483.

40. G.Q. Ma, Z.Y. Wen, J. Jin, Y. Lu, X.W. Wu, M.F. Wu, C.H. Chen, J. Mater. Chem. A 2 (2014) 10350-10354.

41. Y. Liu, W.J. Yan, X.W. An, X. Du, Z.D. Wang, H.L. Fan, S.B. Liu, X.G. Hao, G.Q. Guan, Electrochim. Acta 271 (2018) 67-76.

42. B. Guo, S. Bandaru, C. Dai, H. Chen, Y. Zhang, Q. Xu, S.J. Bao, M. Chen, M. Xu, ACS Appl. Mater. Interfaces 10 (2018) 43707-43715.

43. L. Hu, C. Dai, H. Liu, Y. Li, B. Shen, Y. Chen, S.J. Bao, M. Xu, Adv. Energy Mater. 8 (2018) 1800709.

44. Y. Zhao, W. Zhu, G.Z. Chen, E.J. Cairns, J. Power Sources 327 (2016) 447-456.

45. T. Chen, Z. Zhang, B. Cheng, R. Chen, Y. Hu, L. Ma, G. Zhu, J. Liu, Z. Jin, J. Power Sources 139 (2017) 12710-12715.

46. W.J. Xue, Q.B. Yan, G.Y. Xu, L.M. Suo, Y.M. Chen, C. Wang, C.A. Wang, J. Li, Nano Energy 38 (2017) 12-18.

47. E.H.M. Salhabi, J. Zhao, J. Wang, M. Yang, B. Wang, D. Wang, Angew. Chem. Int. Ed. 58 (2019) 9078-9082.

48. P.C. Du, W.L. Wei, Y.M. Dong, D. Liu, Q. Wang, Y. Peng, S.W. Chen, P. Liu, Nanoscale 11 (2019) 10097-10105.

49. B. Long, Z. Qiao, J. Zhang, S. Zhang, M.S. Balogun, J. Lu, S. Song, Y. Tong, J. Mater. Chem. A 7 (2019) 11370-11378.

50. J. Ni, L.M. Jin, M.Z. Xue, J.S. Zheng, J.P. Zheng, C.M. Zhang, Electrochim. Acta 296 (2019) 39-

48.

51. M.Q. Zhu, S.M. Li, J.H. Liu, B. Li, Appl. Surf. Sci. 473 (2019) 1002-1008.

52. X. Wu, Y. Du, P.X. Wang, L.S. Fan, J.H. Cheng, M.X. Wang, Y. Qiu, B. Guan, H.X. Wu, N.Q. Zhang, K.N. Sun, J. Mater. Chem. A 5 (2017) 25187-25192.

53. C.C. Li, J.J. Shi, L. Zhu, Y.Y. Zhao, J. Lu, L.Q. Xu, Nano Res. 11 (2018) 4302-4312.

54. J. Zhang, H. Hu, Z. Li, X.W. Lou, Angew. Chem. Int. Ed. 55 (2016) 3982-3986.

55. J. Zhang, Z. Li, Y. Chen, S. Gao, X.W. Lou, Angew. Chem. Int. Ed. 57 (2018) 10944-10948.

56. C. Lin, L. Qu, J. Li, Z. Cai, H. Liu, P. He, X. Xu, L. Mai, Nano Res. 12 (2019) 205-210.

57. W.Q. Yao, C.J. Chu, W.Z. Zheng, L. Zhan, Y.L. Wang, J. Mater. Chem. A 6 (2018) 18191-18205.

58. J. Huang, B. Cao, F. Zhao, L. Zhang, Y. Qu, Y. Chen, Electrochim. Acta 304 (2019) 62-69.

59. H. Zhang, Z. Zhao, Y. Hou, Y. Tang, J. Liang, X. Liu, Z. Zhang, X. Wang, J. Qiu, J. Mater. Chem. A 7 (2019) 9230-9240.

60. Y. Tian, H. Huang, G. Liu, R. Bi, L. Zhang, Chem. Commun. 55 (2019) 3243-3246.

61. J. Tu, H. Li, J. Zou, S. Zeng, Q. Zhang, L. Yu, X. Zeng, Dalton Trans. 47 (2018) 16909-16917.

62. S.D. Seo, D. Park, S. Park, D.W. Kim, Adv. Funct. Mater. 29 (2019) 1903712.

63. C. Ye, L. Zhang, C. Guo, D. Li, A. Vasileff, H. Wang, S.Z. Qiao, Adv. Funct. Mater. 27 (2017) 1702524.

64. W. Wu, J. Pu, J. Wang, Z. Shen, H. Tang, Z. Deng, X. Tao, F. Pan, H. Zhang, Adv. Energy Mater. 8 (2018) 1702373.

65. S.K. Wu, Y.Z. Wang, S.S. Na, C.J. Chen, T.F. Yu, H.Y. Wang, H.M. Zang, J. Mater. Chem. A 5 (2017) 17352-17359.

66. B.K. Cao, Y. Chen, D. Li, L.H. Yin, Y. Mo, ChemSusChem 9 (2016) 3338-3344.

67. B. Cao, D. Li, B. Hou, Y. Mo, L. Yin, Y. Chen, ACS Appl. Mater. Interfaces 8 (2016) 27795-27802.

68. J. He, L. Luo, Y. Chen, A. Manthiram, Adv. Mater. 29 (2017) 1702707.

69. G. Zheng, Q. Zhang, J.J. Cha, Y. Yang, W. Li, Z.W. Seh, Y. Cui, Nano Lett. 13 (2013) 1265-1270.

70. Z. Lyu, D. Xu, L. Yang, R. Che, R. Feng, J. Zhao, Y. Li, Q. Wu, X. Wang, Z. Hu, Nano Energy 12 (2015) 657-665.

71. Y. Zhang, G. Li, J. Wang, G. Cui, X. Wei, L. Shui, K. Kempa, G. Zhou, X. Wang, Z. Chen, Adv. Funct. Mater. 30 (2020) 2001165.

72. Z. Sun, S. Vijay, H.H. Heenen, A.Y.S. Eng, W. Tu, Y. Zhao, S.W. Koh, P. Gao, Z.W. Seh, K. Chan, H. Li, Adv. Energy Mater. 10 (2020) 1904010.

73. C. Wang, H. Song, C. Yu, Z. Ullah, Z. Guan, R. Chu, Y. Zhang, L. Zhao, Q. Li, L. Liu, J. Mater. Chem. A 8 (2020) 3421-3430.

74. J. Wang, H. Yang, Z. Chen, L. Zhang, J. Liu, P. Liang, H. Yang, X. Shen, Z.X. Shen, Adv. Sci. 5 (2018) 1800621.

75. P.Z. Lu, F.W. Ye, Q.G. Si, H.Z. Jing, J. Phys. Chem. C 119 (2015) 28721-28727.

76. H. Li, Z. Ge, Y.P. Zheng, Y. Xue, G. Bai, J. Wang, K. Zhuo, Y.J. Wang, Chem. Commun. 55 (2019) 1991-1994.

77. Y. Zhong, L. Qian, Y. Zhu, Y. Zhu, Z. Wei, S. Wang, Z.P. Shao, Adv. Sustain. Syst. 1 (2017) 1700081.

78. S.K. Park, J. Lee, T. Hwang, Y.Z. Piao, J. Mater. Chem. A 5 (2017) 975-981.

79. G.M Zhou, Y.B. Zhao, A. Manthiram, Adv. Energy Mater. 5 (2015) 1402263.

80. M. Zhen, S. Li, H. Ying, X. Xin, X. Zhu, W.Q. Han, Adv. Mater. Interfaces 4 (2017) 1601195.

81. F. Xu, Z. Tang, S. Huang, L. Chen, Y. Liang, W. Mai, H. Zhong, R. Fu, D. Wu, Nat. Commun. 6 (2015) 7221.

82. X. Li, X. Cheng, M. Gao, D. Ren, Y. Liu, Z. Guo, C. Shang, L. Sun, H.G. Pan, ACS Appl. Mater. Interfaces 9 (2017) 10717-10729.

83. G. He, S. Evers, X. Liang, M. Cuisinier, A. Garsuch, L.F. Nazar, ACS Nano 7 (2013) 10920-10930.

84. W. Zhou, C. Wang, Q. Zhang, H.D. Abruña, H. Yang, J. Wang, S.X. Mao, X.C. Xiao, Adv. Energy Mater. 5 (2015) 1401752.

85. W. Zhou, X. Xiao, M. Cai, L. Yang, Nano Lett. 14 (2014) 5250-5256.

86. D. Dutta, S. Gope, D.S. Negi, R. Datta, A.K. Sood, A.J. Bhattacharyya, J. Phys. Chem. C 120 (2016) 29011-29022.

87. D. Gueon, M.Y. Ju, J.H. Moon, Proc. Natl. Acad. Sci. U.S.A. 117 (2020) 12686-12692.

88. G.Y. Zheng, Y. Yuan, J.J. Cha, S.S. Hong, Y. Cui, Nano Lett. 11 (2011) 4462-4467.

89. C. Zhang, H.B. Wu, C. Yuan, Z. Guo, X.W. Lou, Angew. Chem. Int. Ed. 51 (2012) 9592-9595.

90. Y. Qu, Z. Zhang, X. Wang, Y. Lai, Y. Liu, J. Li, J. Mater. Chem. A 1 (2013) 14306-14310.

91. Z. Li, J. Zhang, B. Guan, D. Wang, L.M. Liu, X.W. Lou, Nat. Commun. 7 (2016) 13065.

92. E.P. Barrett, L.G. Joyner, P.P. Halenda, J. Am. Chem. Soc. 73 (1951) 373-380.

93. J. Scholz, B. Kayaalp, A.C. Juhl, D. Clemens, M. Fröba, S. Mascotto, ACS Energy Lett. 3 (2018) 387-392.

94. C.P. Yang, Y.X. Yin, Y.G. Guo, L.J. Wan, J. Am. Chem. Soc. 137 (2015) 2215-2218.

95. L.H. Zhang, B. He, W.C. Li, A.H. Lu, Adv. Energy Mater. 7 (2017) 1701518.

96. Y. Zhong, S. Wang, Y. Sha, M. Liu, R. Cai, L. Li, Z. Shao, J. Mater. Chem. A 4 (2016) 9526-9535.

97. Q. Sun, B. He, X.Q. Zhang, A.H. Lu, ACS Nano 9 (2015) 8504-8513.

98. F.F. Zhang, G. Huang, X.X. Wang, Y.L. Qin, X.C. Du, D.M. Yin, F. Liang, L.M. Wang, Chem. Eur. J. 20 (2014) 17523-17529.

99. K. Zhang, Q. Zhao, Z. Tao, J. Chen, Nano Res. 6 (2013) 38-46.

100. S. Dörfler, M. Hagen, H. Althues, J. Tübke, S. Kaskel, M.J. Hoffmann, Chem. Commun. 48 (2012) 4097-4099.

101. Y. Huang, M. Zheng, Z. Lin, B. Zhao, S. Zhang, J. Yang, C. Zhu, H. Zhang, D. Sun, Y. Shi, J. Mater. Chem. A 3 (2015) 10910-10918.

102. D. Xiao, L. Qian, H. Zhang, Y. Ma, C. Lu, C.M. Chen, Y. Liu, S.X. Yuan, J. Mater. Chem. A 5 (2017) 24901-24908.

103. M. Li, R.E. Carter, A. Douglas, L. Oakes, C.L. Pint, ACS Nano 11 (2017) 4877-4884.

104. R. Carter, L. Oakes, N. Muralidharan, C.L. Pint, J. Phys. Chem. C 121 (2017) 7718-7727.

105. J.Y. Hwang, H.M. Kim, S.K. Lee, J.H. Lee, A. Abouimrane, M.A. Khaleel, I. Belharouak, A. Manthiram, Y.K. Sun, Adv. Energy Mater. 6 (2016) 1501480.

106. N. Jayaprakash, J. Shen, S.S. Moganty, A. Corona, L.A. Archer, Angew. Chem. Int. Ed. 50 (2011) 5904-5908.

107. R. Carter, L. Oakes, N. Muralidharan, A.P. Cohn, A. Douglas, C.L. Pint, ACS Appl. Mater. Interfaces 9 (2017) 7185-7192.

108. X. Liang, L.F. Nazar, ACS Nano 10 (2016) 4192-4198.

109. H. Chen, C. Wang, W. Dong, W. Lu, Z. Du, L. Chen, Nano Lett. 15 (2015) 798-802.

110. W. Li, G. Zheng, Y. Yang, Z.W. Seh, N. Liu, Y. Cui, Proc. Natl. Acad. Sci. U.S.A. 110 (2013) 7148-7153.

111. X. Wang, G. Li, J. Li, Y. Zhang, A. Wook, A. Yu, Z. Chen, Energy Environ. Sci. 9 (2016) 2533-2538.

112. M. Yan, Y. Zhang, Y. Li, Y. Huo, Y. Yu, C. Wang, J. Jin, L. Chen, T. Hasan, B. Wang, B.L. Su, J. Mater. Chem. A 4 (2016) 9403-9412.

113. W. Zhou, Y. Yu, H. Chen, F.J. DiSalvo, H.D. Abruña, J. Am. Chem. Soc. 135 (2013) 16736-16743.

114. Y. Ansari, S. Zhang, B. Wen, F. Fan, Y.M. Chiang, Adv. Energy Mater. 9 (2019) 1802213.

115. Y. Deng, H. Xu, Z. Bai, B. Huang, J. Su, G.H. Chen, J. Power Sources 300 (2015) 386-394.

116. K. Cao, H. Liu, Y. Li, Y. Wang, L. Jiao, Energy Stor. Mater. 9 (2017) 78-84.

117. L. Ni, Z. Wu, G. Zhao, C. Sun, C. Zhou, X. Gong, G. Diao, Small 13 (2017) 1603466.

118. W. Tang, Z. Chen, B. Tian, H.W. Lee, X. Zhao, X. Fan, Y. Fan, K. Leng, C. Peng, M.H. Kim, M. Li, M. Lin, J. Su, J. Chen, H.Y. Jeong, X. Yin, Q. Zhang, W. Zhou, K.P. Loh, G.W. Zheng, J. Am. Chem. Soc. 139 (2017) 10133-10141.

119. X.M. Liu, C.L. Meng, P.B. Gao, S.H. Zhuang, H. Tang, Z.H. Bao, RSC Adv. 6 (2016) 1902-1906.

120. Y. Song, J. Tan, G. Wang, P. Gao, J. Lei, L. Zhou, Chem. Sci. 11 (2020) 772-777.

121. Y. Xia, M. Wei, Y. Lu, Synth. Met. 159 (2009) 372-376.

122. X. Zhou, F. Chen, J. Yang, J. Energy Chem. 24 (2015) 448-455.

123. H. Wang, Y. Yang, Y. Liang, J.T. Robinson, Y. Li, A. Jackson, Y. Cui, H. Dai, Nano Lett. 11 (2011) 2644-2647.

124. M. Zhang, Q. Meng, A. Ahmad, L. Mao, W. Yan, Z. Wei, J. Mater. Chem. A 5 (2017) 17647-17652.

125. Y. Fu, A. Manthiram, J. Phys. Chem. C 116 (2012) 8910-8915.

126. M.J.H. Worthington, R.L. Kucera, J.M. Chalker, Green Chem. 19 (2017) 2748-2761.

127. D.A. Boyd, Angew. Chem. Int. Ed. 55 (2016) 15486-15502.

128. L. Huang, J. Cheng, X. Li, D. Yuan, W. Ni, G. Qu, Q. Guan, Y. Zhang, B. Wang, J. Mater. Chem. 3 (2015) 4049-4057.

129. Z. Meng, S. Zhang, J. Wang, X. Yan, H. Ying, X. Xu, W. Zhang, X. Hou, W.Q. Han, ACS Appl. Energy Mater. 1 (2018) 1594-1602.

130. X. Fan, Y. Zhang, J. Li, K. Yang, Z. Liang, Y. Chen, C. Zhao, Z. Zhang, K. Mai, J. Mater. Chem. A 6 (2018) 11664-11669.

131. G. Qu, J. Cheng, X. Li, L. Huang, W. Ni, Z. Wang, B. Wang, ACS Appl. Mater. Interfaces 7 (2015) 16668-16675.

132. H. Chen, W. Dong, J. Ge, C. Wang, X. Wu, W. Lu, L. Chen, Sci. Rep. 3 (2013) 1910.

133. X.Y. Xie, L.Y. Li, P.S. Zheng, W.J. Zheng, Y. Bai, T.F. Cheng, J. Liu, Mater. Res. Bull. 47 (2012) 3665-3669.

134. L. Sun, D.T. Wang, Y.F. Luo, K.B. Wang, W.B. Kong, Y. Wu, L.N. Zhang, K.L. Jiang, Q.Q. Li, Y.H. Zhang, J.P. Wang, S.S. Fan, ACS Nano 10 (2016) 1300-1308.

135. X.Q. Zhang, D. Xie, Y. Zhong, D.H. Wang, J.B. Wu, X.L. Wang, X.H. Xia, C.D. Gu, J.P. Tu, Chem. Eur. J. 23 (2017) 10610-10615.

136. Z.J. Fan, B. Ding, H.S. Guo, M.Y. Shi, Y.D. Zhang, S.Y. Dong, T.F. Zhang, H. Dou, X.J. Zhang, Chem. Eur. J. 25 (2019) 10710-10717.

137. J. Xu, J. Shui, J. Wang, M. Wang, H.K. Liu, S.X. Dou, I.Y. Jeon, J.M. Seo, J.B. Baek, L. Dai, ACS Nano 8 (2014) 10920-10930.

138. S. Zellmer, P. Titscher, E. Wienken, A. Kwade, G. Garnweitner, Energy Stor. Mater. 9 (2017) 70-77.

139. C. Wang, H. Chen, W. Dong, J. Ge, W. Lu, X. Wu, L. Guo, L. Chen, Chem. Commun. 50 (2014) 1202-1204.

140. Y. Xie, H. Zhao, H. Cheng, C. Hu, W. Fang, J. Fang, J. Xu, Z. Chen, Appl. Energy 175 (2016) 522-528.

141. J. Shao, X. Li, L. Zhang, Q. Qu, H. Zheng, Nanoscale 5 (2013) 1460-1464.

142. X. Wang, Z. Zhang, X. Yan, Y. Qu, Y. Lai, J. Li, Electrochim. Acta 155 (2015) 54-60.

143. N. Díez, G.A. Ferrero, M. Sevilla, A.B. Fuertes, Sustain. Energy Fuels 3 (2019) 3498-3509.

144. S. Evers, L.F. Nazar, Chem. Commun. 48 (2012) 1233-1235.

145. J. Zhao, Z.F. Fan, Microchim. Acta 187 (2020) 3.

146. S. Wang, X. Bao, B. Gao, M. Li, Dalton Trans. 48 (2019) 8288-8296.

147. Q.L. Li, L.X. Shi, K. Du, Y. Qin, S.J. Qu, D.Q. Xia, Z. Zhou, Z.G. Huang, S.N. Ding, ACS Omega 5 (2020) 5407-5411.

148. L. Fu, A. Wang, K. Xie, J. Zhu, F. Chen, H. Wang, H. Zhang, W. Su, Z. Wang, C. Zhou, S. Ruan, Sens. Actuators B Chem. 304 (2020) 127390.

149. H. Wang, Z. Wang, Y. Xiong, S.V. Kershaw, T. Li, Y. Wang, Y. Zhai, A.L. Rogach, Angew. Chem. Int. Ed. 58 (2019) 7040-7044.

150. L. Shen, H. Wang, S. Liu, Z. Bai, S. Zhang, X. Zhang, C. Zhang, J. Am. Chem. Soc. 140 (2018) 7878-7884.

151. G. Qiao, L. Liu, X. Hao, J. Zheng, W. Liu, J. Gao, C.C. Zhang, Q. Wang, Chem. Eng. J. 382 (2020) 122907.

152. Z. Wang, C. Zhang, H. Wang, Y. Xiong, X. Yang, Y.E. Shi, A.L. Rogach, Angew. Chem. Int. Ed. 59 (2020) 9997-10002.

153. F. Arshad, M.P. Sk, ACS Appl. Nano Mater. 3 (2020) 3044-3049.

154. Y.X. Mo, Y.H. Jiang, J.X. Lin, Y. Zhou, J.T. Li, Q.H. Wu, L. Huang, H.G. Liao, S.G. Sun, ChemElectroChem 5 (2018) 1683-1690.

155. G. Yuan, H.D. Wang, J. Energy Chem. 23 (2014) 657-661.

156. Y.Z. Fu, A. Manthiram, RSC Adv. 2 (2012) 5927-5929.

157. J. Wang, J. Chen, K. Konstantinov, L. Zhao, S.H. Ng, G.X. Wang, Z.P. Guo, H.K. Liu, Electrochim.

Acta 51 (2006) 4634-4638.

158. K.L. Zhang, Y.H. Xu, Y. Lu, Y.C. Zhu, Y.Y. Qian, D.F. Wang, J.B. Zhou, N. Lin, Y.T. Qian, J. Mater. Chem. A 4 (2016) 6404-6410.

159. H. Hu, H. Cheng, Z. Liu, G. Li, Q. Zhu, Y. Yu, Nano Lett. 15 (2015) 5116-5123.

160. F. Wu, J. Chen, R. Chen, S. Wu, L. Li, S. Chen, T. Zhao, J. Phys. Chem. 115 (2011) 6057-6063.

161. W. Li, Q. Zhang, G. Zheng, Z.W. Seh, H. Yao, Y. Cui, Nano Lett. 13 (2013) 5534-5540.

162. M. Zhu, S. Li, B. Li, S. Yang, Nanoscale 11 (2019) 412-417.

163. Y.X. Mo, J.X. Lin, Y.J. Wu, Z.W. Yin, Y.Q. Lu, J.T. Li, Y. Zhou, T. Sheng, L. Huang, S.G. Sun, ACS Appl. Mater. Interfaces 11 (2019) 4065-4073.

164. L. Zhang, Z. Chen, N. Dongfang, M. Li, C. Diao, Q. Wu, X. Chi, P. Jiang, Z. Zhao, L. Dong, R. Che, K.P. Loh, H. Lu, Adv. Energy Mater. 8 (2018) 1802431.

165. L.Y. Hu, C.L. Dai, J.M. Lim, Y.M. Chen, X. Lian, M.Q. Wang, Y. Li, P.H. Xiao, G. Henkelman, M.W. Xu, Chem. Sci. 9 (2018) 666-675.

166. S. Rehman, T. Tang, Z. Ali, X. Huang, Y. Hou, Small 13 (2017) 1700087.

167. X. Liang, Y. Liu, Z. Wen, L. Huang, X. Wang, H. Zhang, J. Power Sources 196 (2011) 6951-6955.

168. X. Zhao, H.J. Ahn, K.W. Kim, K.K. Cho, J.H. Ahn, J. Phys. Chem. C 119 (2015) 7996-8003.

169. D. Su, M. Cortie, H. Fan, G. Wang, Adv. Mater. 29 (2017) 1700587.

170. N. Osada, C.B. Bucur, H. Aso, J. Muldoon, Energy Environ. Sci. 9 (2016) 1668-1673.

171. C.B. Bucur, J. Muldoon, A. Lita, Energy Environ. Sci. 9 (2016) 992-998.

172. F. He, J. Ye, Y. Cao, L. Xiao, H. Yang, X. Ai, ACS Appl. Mater. Interfaces 9 (2017) 11626-11633.

173. Z. Chang, H. Dou, B. Ding, J. Wang, Y. Wang, G. Xu, C. Li, New J. Chem. 40 (2016) 7680-7686.

174. H. Li, M. Sun, T. Zhang, Y. Fang, G. Wang, J. Mater. Chem. A 2 (2014) 18345-18352.

175. P. Xiao, F. Bu, G. Yang, Y. Zhang, Y. Xu, Adv. Mater. 29 (2017) 1703324.

176. Q. Zhao, X. Hu, K. Zhang, N. Zhang, Y. Hu, J. Chen, Nano Lett. 15 (2015) 721-726.

177. J. Liu, L. Yuan, K. Yuan, Z. Li, Z. Hao, J. Xiang, Y. Huang, Nanoscale 8 (2016) 13638-13645.

178. H. Wang, Q. Zhang, H. Yao, Z. Liang, H.W. Lee, P.C. Hsu, G. Zheng, Y. Cui, Nano Lett. 14 (2014) 7138-7144.

179. H. Lin, L. Yang, X. Jiang, G. Li, T. Zhang, Q. Yao, G.W. Zheng, J.Y. Lee, Energy Environ. Sci. 10 (2017) 1476-1486.

180. Y.H. Ding, Y. Chen, N. Xu, X.T. Lian, L.L. Li, Y.X. Hu, S.J. Peng, Nano-Micro Lett. 12 (2020) 54.

181. S. Zhang, D. Xu, C. Su, W. Tang, H. Ju, J. Zhang, B. Tian, Chem. Commun. 56 (2020) 810-813.

182. R. Liu, F. Ren, W. Su, P. He, C. Shen, L. Zhang, C.A. Wang, Ceram. Int. 41 (2015) 14615-14620.

183. H. Fan, Q. Tang, X. Chen, B. Fan, S. Chen, A. Hu, Chem. Asian J. 11 (2016) 2911-2917.

184. C.L. Chang, H.S. Fogler, M.N. Blanco, Langmuir 13 (1997) 3295-3307.

185. Z.W. Seh, W. Li, J.J. Cha, G. Zheng, Y. Yang, M.T. McDowell, P.C. Hsu, Y. Cui, Nat. Commun. 4 (2013) 1331.

186. B. Campbell, J. Bell, H. Hosseini Bay, Z. Favors, R. Ionescu, C.S. Ozkan, M. Ozkan, Nanoscale 7 (2015) 7051-7055.

187. T. Liu, X. Sun, S. Sun, Q. Niu, H. Liu, W. Song, F. Cao, X. Li, T. Ohsaka, J. Wu, Electrochim. Acta 295 (2019) 684-692.

188. M. Fang, Z. Chen, Y. Liu, J. Quan, C. Yang, L. Zhu, Q. Xu, Q. Xu, J. Mater. Chem. A 6 (2018) 1630-1638.

189. S. Huang, L. Liu, Y. Wang, Y. Shang, L. Zhang, J. Wang, Y. Zheng, O.G. Schmidt, H.Y. Yang, J. Mater. Chem. A 7 (2019) 6651-6658.

190. X. Liang, C. Hart, Q. Pang, A. Garsuch, T. Weiss, L.F. Nazar, Nat. Commun. 6 (2015) 5682.

191. M. Chen, Q. Lu, S. Jiang, C. Huang, X. Wang, B. Wu, K. Xiang, Y. Wu, Chem. Eng. J. 335 (2018) 831-842.

192. J. Zhang, Y. Shi, Y. Ding, W. Zhang, G. Yu, Nano Lett. 16 (2016) 7276-7281.

193. J. Wu, Q. Ma, C. Lian, Y. Yuan, D. Long, Chem. Eng. J. 370 (2019) 556-564.

194. L. Ni, G. Zhao, G. Yang, G. Niu, M. Chen, G. Diao, ACS Appl. Mater. Interfaces 9 (2017) 34793-34803.

195. G. Greczynski, L. Hultman, Angew. Chem. Int. Ed. 59 (2020) 5002-5006.

196. S. Chen, Z. Wu, J. Luo, X. Han, J. Wang, Q. Deng, Z. Zeng, S. Deng, Electrochim. Acta 312 (2019) 109-118.

197. J.Y. Hwang, H.M. Kim, S. Shin, Y.K. Sun, Adv. Funct. Mater. 28 (2018) 1704294.

198. C. Dai, L. Hu, M.Q. Wang, Y. Chen, J. Han, J. Jiang, Y. Zhang, B. Shen, Y. Niu, S.J. Bao, M. Xu, Energy Stor. Mater. 8 (2017) 202-208.

199. H.J. Peng, Z.W. Zhang, J.Q. Huang, G. Zhang, J. Xie, W.T. Xu, J.L. Shi, X. Chen, X.B. Cheng, Q. Zhang, Adv. Mater. 28 (2016) 9551-9558.

200. J. Jiang, J. Zhu, W. Ai, X. Wang, Y. Wang, C. Zou, W. Huang, T. Yu, Nat. Commun. 6 (2015) 8622.

201. H. Wu, Y. Li, J. Ren, D. Rao, Q. Zheng, L. Zhou, D. Lin, Nano Energy 55 (2019) 82-92.

202. X. Liang, C.Y. Kwok, F. Lodi-Marzano, Q. Pang, M. Cuisinier, H. Huang, C.J. Hart, D. Houtarde, K. Kaup, H. Sommer, T. Brezesinski, J. Janek, L.F. Nazar, Adv. Energy Mater. 6 (2016) 1501636.

203. J. Liu, J. Shen, Z. Liu, R. Hu, J. Liu, M. Zhu, Chem. Eur. J. 24 (2018) 4573-4582.

204. T. Ma, F. Zhou, T.W. Zhang, H.B. Yao, T.Y. Su, Z.L. Yu, Y. Li, L.L. Lu, S.H. Yu, Angew. Chem. Int. Ed. 56 (2017) 11836-11840.

205. Q. Wang, Z.B. Wang, C. Li, D.M. Gu, J. Mater. Chem. A 5 (2017) 6052-6059.

206. Z.J. Guo, X.Y. Feng, X.X. Li, X.M. Zhang, X. Peng, H. Song, J.J. Fu, K. Ding, X. Huang, B. Gao, Front. Chem. 6 (2018) 429.

207. N. Ding, Y. Lum, S. Chen, S.W. Chien, T.S.A. Hor, Z. Liu, Y. Zong, J. Mater. Chem. A 3 (2015) 1853-1857.

208. J. Cai, Z. Zhang, S. Yang, Y. Min, G. Yang, K. Zhang, Electrochim. Acta 295 (2019) 900-909.

209. Y. Shi, W. Lv, S. Niu, Y. He, G. Zhou, G. Chen, B. Li, Q.H. Yang, F. Kang, Chem. Asian J. 11 (2016) 1343-1347.

210. Q. Wang, Z.B. Wang, R. Li, H. Liu, M. Yang, C. Li, D.M. Gu, Chem. Eng. J. 345 (2018) 271-279.

211. Q. Wang, Z.B. Wang, M. Yang, C. Li, D.M. Gu, J. Mater. Chem. A 5 (2017) 16796-16802.

212. T.Z. Hou, W.T. Xu, X. Chen, H.J. Peng, J.Q. Huang, Q. Zhang, Angew. Chem. Int. Ed. 56 (2017) 8178-8182.

213. T.Z. Hou, X. Chen, H.J. Peng, J.Q. Huang, B.Q. Li, Q. Zhang, B. Li, Small 12 (2016) 3283-3291.

214. G. Li, J. Sun, W. Hou, S. Jiang, Y. Huang, J. Geng, Nat. Commun. 7 (2016) 10601.

215. F.D. Han, J. Yue, X. Fan, T. Gao, C. Luo, Z. Ma, L. Suo, C.S. Wang, Nano Lett. 16 (2016) 4521-4527.

216. L. Zhan, C. Nan, Y. Ye, J. Guo, J. Zhu, E.J. Cairns, Nano Energy 9 (2014) 408-416.

217. S. Liang, C. Liang, Y. Xia, H. Xu, H. Huang, X. Tao, Y. Gan, W. Zhang, J. Power Sources 306 (2016) 200-207.

218. D. Sun, Y. Hwa, L. Zhang, J. Xiang, J. Guo, Y. Huang, E.J. Cairns, Nano Energy 64 (2019) 103891.

219. C. Nan, Z. Lin, H. Liao, M.K. Song, Y. Li, E.J. Cairns, J. Am. Chem. Soc. 136 (2014) 4659-4663.

220. S. Li, D. Leng, W. Li, L. Qie, Z. Dong, Z. Cheng, Z. Fan, Energy Stor. Mater. 27 (2020) 279-296.

221. D. Sun, Y. Hwa, Y. Shen, Y. Huang, E.J. Cairns, Nano Energy 26 (2016) 524-532.

222. D.H. Wang, D. Xie, T. Yang, Y. Zhong, X.L. Wang, X.H. Xia, C.D. Gu, J.P. Tu, J. Power Sources 313 (2016) 233-239.

223. X. Li, M. Gao, W. Du, B. Ni, Y. Wu, Y. Liu, C. Shang, Z. Guo, H. Pan, J. Mater. Chem. A 5 (2017) 6471-6482.

224. L. Xiao, Y. Cao, J. Xiao, B. Schwenzer, M.H. Engelhard, L.V. Saraf, Z. Nie, G.J. Exarhos, J. Liu, Adv. Mater. 24 (2012) 1176-1181.

225. G.C. Li, G.R. Li, S.H. Ye, X.P. Gao, Adv. Energy Mater. 2 (2012) 1238-1245.

226. F. Wu, J. Chen, L. Li, T. Zhao, R. Chen, J. Phys. Chem. C 115 (2011) 24411-24417.

227. G. Ma, Z. Wen, J. Jin, Y. Lu, K. Rui, X. Wu, M. Wu, J. Zhang, J. Power Sources 254 (2014) 353-359.

228. X.Q. Niu, X.L. Wang, D.H. Wang, Y. Li, Y.J. Zhang, Y.D. Zhang, T. Yang, T. Yu, J.P. Tu, J. Mater. Chem. A 3 (2015) 17106-17112.

229. X.Q. Niu, X.L. Wang, D. Xie, D.H. Wang, Y.D. Zhang, Y. Li, T. Yu, J.P. Tu, ACS Appl. Mater. Interfaces 7 (2015) 16715-16722.

230. X.G. Li, M.M. Rao, D.R. Chen, H.B. Lin, Y.L. Liu, Y.H. Liao, L.D. Xing, W.S. Li, Electrochim. Acta 166 (2015) 93-99.

231. W. Yang, W. Yang, J. Feng, X. Qin, J. Energy Chem. 27 (2018) 813-819.

232. L. Lin, F. Pei, J. Peng, A. Fu, J. Cui, X. Fang, N. Zheng, Nano Energy 54 (2018) 50-58.

233. Y.H. Ge, Z. Chen, S.J. Ye, Z.F. Zhu, Y.F. Tu, X.M. Yang, J. Mater. Chem. A 6 (2018) 14885-14893.

234. Z. Li, J. Zhang, X.W. Lou, Angew. Chem. Int. Ed. 54 (2015) 12886-12890.

235. F. Wu, J. Li, Y. Su, J. Wang, W. Yang, N. Li, L. Chen, S. Chen, R. Chen, L. Bao, Nano Lett. 16

(2016) 5488-5494.

236. S.W. Lee, B.S. Kim, S. Chen, Y. Shao-Horn, P.T. Hammond, J. Am. Chem. Soc. 131 (2009) 671-679.

237. R.M. Jisr, H.H. Rmaile, J.B. Schlenoff, Angew. Chem. Int. Ed. 44 (2005) 782-785.

238. Y. Zhao, Y. Meng, P. Jiang, J. Power Sources 259 (2014) 219-226.

239. Y. Li, B. Shi, W. Liu, R. Guo, H. Pei, D. Ye, J. Xie, J. Kong, Electrochim. Acta 260 (2018) 912-920.

240. M.X. He, P.J. Zuo, H. Zhang, J.F. Hua, Y.L. Ma, C.Y. Du, X.Q. Cheng, Y.Z. Gao, G.P. Yin, Electrochim. Acta 259 (2018) 440-448.

241. C. Luo, Y.X. Yan, Y.H. Wan, J.W. Hao, X.M. Liu, H. Yang, Energy Technol. 7 (2019) 201-208.

242. Z. Li, M.S. Pan, L. Su, P.C. Tsai, A.F. Badel, J.M. Valle, S.L. Eiler, K. Xiang, F.R. Brushett, Y.M. Chiang, Joule 1 (2017) 306-327.

243. W. Chen, T. Lei, C. Wu, M. Deng, C. Gong, K. Hu, Y. Ma, L. Dai, W. Lv, W. He, X. Liu, J. Xiong, C. Yan, Adv. Energy Mater. 8 (2018) 1702348.

244. S. Yun, S. H. Park, J. S. Yeon, J. Park, M. Jana, J. Suk, H. Park, Adv. Funct. Mater. 28 (2018) 1707593.

245. N. Li, Z. Weng, Y. Wang, F. Li, H.M. Cheng, H. Zhou, Energy Environ. Mater. 7 (2014) 3307-3312.

246. R. Demir-Cakan, M. Morcrette, J.B. Leriche, J.M. Tarascon, J. Mater. Chem. A 2 (2014) 9025-9029.

247. R. Demir-Cakan, M. Morcrette, J.M. Tarascon, J. Mater. Chem. A 3 (2015) 2869-2875.

248. X. Wu, X. Yuan, J. Yu, J. Liu, F. Wang, L. Fu, W. Zhou, Y. Zhu, Q. Zhou, Y. Wu, Nanoscale 9 (2017) 11004-11011.

249. C. Yang, L. Suo, O. Borodin, F. Wang, W. Sun, T. Gao, X. Fan, S. Hou, Z. Ma, K. Amine, K. Xu, C. Wang, Proc. Natl. Acad. Sci. U.S.A. 114 (2017) 6197-6202.

250. S.S. Zhang, Electrochim. Acta 70 (2012) 344-348.

251. X. Li, M. Banis, A. Lushington, X. Yang, Q. Sun, Y. Zhao, C. Liu, Q. Li, B. Wang, W. Xiao, C. Wang, M. Li, J. Liang, R. Li, Y. Hu, L. Goncharova, H. Zhang, T.K. Sham, X. Sun, Nat. Commun. 9 (2018) 4509.

252. T. Yim, M.S. Park, J.S. Yu, K.J. Kim, K.Y. Im, J.H. Kim, G. Jeong, Y.N. Jo, S.G. Woo, K.S. Kang, I. Lee, Y.J. Kim, Electrochim. Acta 107 (2013) 454-460.

253. J. Balach, T. Jaumann, L. Giebeler, Energy Storage Mater. 8 (2017) 209-216.

254. P.P.R.M.L. Harks, C.B. Robledo, T.W. Verhallen, P.H.L. Notten, F.M. Mulder, Adv. Energy Mater. 7 (2016) 1601635.

255. C. Hu, H. Chen, Y. Shen, D. Lu, Y. Zhao, A. Lu, X. Wu, W. Lu, L. Chen, Nat. Commun. 8 (2017) 479.

256. C. Li, A.L. Ward, S.E. Doris, T.A. Pascal, D. Prendergast, B.A. Helms, Nano Lett. 15 (2015) 5724-5729.

257. F. Huang, L. Gao, Y. Zou, G. Ma, J. Zhang, S. Xu, Z. Li, X. Liang, J. Mater. Chem. A 7 (2019) 12498-12506.

258. M. Helen, M.A. Reddy, T. Diemant, U. Golla-Schindler, R.J. Behm, U. Kaiser, M. Fichtner, Sci. Rep. 5 (2015) 12146.

259. S. Xin, L. Gu, N.H. Zhao, Y.X. Yin, L.J. Zhou, Y.G. Guo, L.J. Wan, J. Am. Chem. Soc. 134 (2012) 18510-18513.

260. M. Helen, T. Diemant, S. Schindler, R.J. Behm, M. Danzer, U. Kaiser, M. Fichtner, M. Anji Reddy, ACS Omega 3 (2018) 11290-11299.

261. F. Jin, C. Hu, C. Liu, Y. Zheng, H. Chen, Y. Shen and L. Chen, J. Electroanal. Chem. 835 (2019)

156-160.